

# The PyCASSO database: Spatially resolved stellar population properties for CALIFA galaxies

A. L. de Amorim,<sup>1\*</sup> R. García-Benito,<sup>2</sup> R. Cid Fernandes,<sup>1</sup> C. Cortijo-Ferrero,<sup>2</sup>  
R. M. González Delgado,<sup>2</sup> E. A. D. Lacerda,<sup>1</sup> R. López Fernández,<sup>2</sup> E. Pérez,<sup>2</sup>  
and N. Vale Asari<sup>1</sup>

<sup>1</sup>*Departamento de Física, Universidade Federal de Santa Catarina, P.O. Box 476, 88040-900, Florianópolis, SC, Brazil*

<sup>2</sup>*Instituto de Astrofísica de Andalucía (CSIC), P.O. Box 3004, 18080 Granada, Spain.*

Accepted XXX. Received YYY; in original form ZZZ

## ABSTRACT

The Calar Alto Legacy Integral Field Area (CALIFA) survey, a pioneer in integral field spectroscopy legacy projects, has fostered many studies exploring the information encoded on the spatially resolved data on gaseous and stellar features in the optical range of galaxies. We describe a value-added catalogue of stellar population properties for CALIFA galaxies analysed with the spectral synthesis code STARLIGHT and processed with the PyCASSO platform. Our public data base (<http://pycasso.ufsc.br/>, mirror at <http://pycasso.iaa.es/>) comprises 445 galaxies from the CALIFA Data Release 3 with COMBO data. The catalogue provides maps for the stellar mass surface density, mean stellar ages and metallicities, stellar dust attenuation, star formation rates, and kinematics. Example applications both for individual galaxies and for statistical studies are presented to illustrate the power of this data set. We revisit and update a few of our own results on mass density radial profiles and on the local mass–metallicity relation. We also show how to employ the catalogue for new investigations, and show a pseudo Schmidt–Kennicutt relation entirely made with information extracted from the stellar continuum. Combinations to other databases are also illustrated. Among other results, we find a very good agreement between star formation rate surface densities derived from the stellar continuum and the H $\alpha$  emission. This public catalogue joins the scientific community’s effort towards transparency and reproducibility, and will be useful for researchers focusing on (or complementing their studies with) stellar properties of CALIFA galaxies.

**Key words:** galaxies: evolution – galaxies: stellar content – galaxies: star formation – techniques: imaging spectroscopy – catalogues

## 1 INTRODUCTION

The *modus operandi* of extragalactic astrophysics was transformed by large spectroscopic surveys, such as the 2dF Galaxy Redshift Survey (Colless et al. 2001) and the Sloan Digital Sky Survey (SDSS; York et al. 2000). Instead of relying on a few dozen galaxies, now hundreds of thousands are routinely summoned to address a wide variety of astrophysical questions. The combination of large surveys with stellar population libraries with good spectral resolution (e.g. Bruzual & Charlot 2003) was the cornerstone for the uprise of several spectral synthesis codes, such as our own code STARLIGHT (Cid Fernandes et al. 2005), and those by other

groups: MOPED (Panter et al. 2003), STECMAP/STECKMAP (Ocvirk et al. 2006a,b), VESPA (Tojeiro et al. 2007), ULYSS (Koleva et al. 2008).

One example of the statistical power of applying STARLIGHT to a million SDSS galaxy spectra was revealing a huge and forgotten population of retired galaxies ionized by hot low mass evolved stars, whose spectra are confounded with those of low ionization nuclear emission regions (Stasińska et al. 2008; Cid Fernandes et al. 2010, 2011). This population completely changes the census of galaxies in the local universe (Stasińska et al. 2015). Other examples include studies of the stellar mass–metallicity relation (Vale Asari et al. 2009), the chemical evolution and the star formation history of local galaxies (Cid Fernandes et al. 2007; Asari et al. 2007), how to distinguish AGN hosts (Stasińska et al. 2006), the bimodality of galaxies and the downsizing

\* E-mail: andre@astro.ufsc.br

(Mateus et al. 2006), and the dependence of galaxy properties on the environment (Mateus et al. 2007). More importantly in the context of this paper, the data and tools behind these studies were made publicly available, fostering independent research. Since having published our value-added STARLIGHT-SDSS catalogue (Cid Fernandes et al. 2009) in a public database (<http://starlight.ufsc.br>), studies like Bian et al. (2007); Liang et al. (2007); Peebles et al. (2009); Riffel et al. (2009); Lara-López et al. (2009a,b, 2010); Andrews & Martini (2013) have used our code and database.

These past few years have witnessed the surge of integral field spectroscopy (IFS) observations. While SDSS obtained one spectrum per galaxy, IFS surveys commit to spectrally map galaxies pixel by pixel. The Calar Alto Legacy Integral Field Survey Area survey (CALIFA; Sánchez et al. 2012) was a pioneer wide-field IFS survey of nearby galaxies. Its Data Release 3 (DR3; Sánchez et al. 2016c) contains 445 galaxy COMBO data cubes covering 3700–7500 Å and in the redshift range  $0.005 < z < 0.03$ . The COMBO cubes have a resolution of 850, approximately FWHM = 6 Å at  $\lambda = 5000$  Å. The spatial sampling is 1'', with a PSF given by a Moffat profile with FWHM = 2.5'' and  $\beta = 2$ . CALIFA provides a statistically significant sample which is complete in the magnitude range  $-19.0 < M_r < -23.1$  and stellar masses<sup>1</sup> between  $10^{9.7}$  and  $10^{11.4} M_{\odot}$  (Walcher et al. 2014). In addition to its clear selection criteria, another characteristic that sets CALIFA apart is its spatial coverage ( $> 2$  half light radius), which maps galaxies farther in their outskirts than other ongoing surveys such as SAMI (Croom et al. 2012) and MaNGA (Bundy et al. 2015).

We have analysed the CALIFA data cubes with our spectral synthesis code STARLIGHT and the Python CALIFA STARLIGHT Synthesis organiser (PyCASSO) platform, as described in Cid Fernandes et al. (2013, 2014). This formed the basis of a series of studies about the spatially resolved stellar population properties, where we have obtained:

(i) Evolutionary curves of the cumulative mass function, tracing the mass assembly history of  $\sim 100$  galaxies as a function of the radial distance (Pérez et al. 2013). The results suggest that galaxies grow inside-out, as confirmed by García-Benito et al. (in prep.) for a seven times larger sample.

(ii) 2D maps and spatially resolved information of the stellar populations properties, used to retrieve the local relations between: a) stellar mass surface density,  $\Sigma_{\star}$ , and luminosity weighted stellar ages,  $\langle \log t \rangle_L$  (González Delgado et al. 2014a); b) mass weighted stellar metallicity,  $\langle \log Z \rangle_M$ , and  $\Sigma_{\star}$  (González Delgado et al. 2014b); c) the intensity of the star formation rate,  $\Sigma_{\text{SFR}}$ , defined in this work as the star formation rate surface density, and  $\Sigma_{\star}$  (González Delgado et al. 2016). These relations indicate that local processes are relevant to regulate the star formation and chemical enrichment in the disk of spirals. For spheroids, on the other hand, the stellar mass,  $M_{\star}$ , regulates these processes.

(iii) Radial profiles of stellar extinction,  $A_V$ ,  $\Sigma_{\star}$ ,  $\langle \log t \rangle_L$ ,  $\langle \log Z \rangle_M$ , and their radial gradients also confirm that more massive galaxies are more compact, older, metal rich, and less reddened by dust. These trends are preserved spatially

as a function of the radial distance to the nucleus. Deviations from these relations seem to be correlated with Hubble type: earlier types are more compact, older, and more metal rich for a given  $M_{\star}$ , which evidences that the shut down of the star formation is related to galaxy morphology (González Delgado et al. 2015a). The negative radial gradients of  $\langle \log t \rangle_L$  and  $\langle \log Z \rangle_M$  also confirm that galaxies grow inside-out.

(iv) The radial profiles of  $\Sigma_{\text{SFR}}$  and the small dispersion between the profiles of late type spirals (Sbc, Sc, Sd) confirm that the main sequence of the star forming galaxies is a sequence with nearly constant  $\Sigma_{\text{SFR}}$  (González Delgado et al. 2016). Furthermore, the radial profiles of local and recent specific star formation rate depend on Hubble type (increasing as one goes from early to late types) and increase radially outwards. This behavior suggests that galaxies are quenched inside-out, and that this process is faster in the central bulge-dominated parts than in the disks (González Delgado et al. 2016).

(v) From the 2D ( $R \times t$ ) map of the galaxy SFH we retrieve the spatially resolved time evolution information of the star formation rate (SFR), its intensity ( $\Sigma_{\text{SFR}}$ ), and specific star formation (sSFR). We find that galaxies form very fast independently of their stellar mass, with the peak of star formation at high redshift ( $z > 2$ ), and that subsequent star formation is driven by  $M_{\star}$  and morphology, with less massive and later type spirals showing more prolonged periods of star formation (González Delgado et al. 2017, submitted).

(vi) From the comparison of the spatially resolved and the integrated spectra analyses, we find that the stellar population properties are well represented by their values at one half light radius (González Delgado et al. 2014a).

(vii) Detailed studies of a small sample of galaxies are very well served by the CALIFA survey and our analysis. For example, the analysis of the spatially resolved SFH of mergers (Cortijo-Ferrero et al. 2017; Cortijo-Ferrero et al. 2017b, 2017c, in prep.) in comparison with “non-interacting” spiral galaxies allows us to estimate the effect of the merger phase in the enhancement of the star formation and their spatial extent, as well as to trace the merger epochs.

(viii) By extending STARLIGHT to combine CALIFA optical spectra and GALEX (Martin et al. 2005) UV photometric data, the uncertainties in stellar properties become smaller (López Fernández et al. 2016). Also, young stellar populations are better constrained, especially for low mass late-type galaxies, where there is a significant  $< 300$  Myr population.

(ix) The well defined selection function of the survey allows for reliable volume corrections (Walcher et al. 2014). Combining these with our homogeneous analysis led to an estimation of the SFR density of the Local Universe of  $0.0105 \pm 0.0008 M_{\odot} \text{ yr}^{-1} \text{ Mpc}^{-3}$ , in agreement with independent estimates (González Delgado et al. 2016; see also López Fernández et al., in prep.).

We release the data used in those papers in a public value-added catalogue (<http://pycasso.ufsc.br/>, mirror at <http://pycasso.iaa.es/>). The data were updated to the latest CALIFA release (DR3) and reduction pipeline (v2.2). Stellar population models used in the STARLIGHT fits were also updated. These modifications have only minor effects with respect to the results reported in the studies mentioned

<sup>1</sup> Assuming a Salpeter IMF.

above. Still, when exemplifying the use of this new database we will take the opportunity to revisit and update some of our previous results.

In addition to embracing the ethos of open science data and tools to encourage reproducible results, our CALIFA-STARLIGHT value-added catalogue can be used for many different purposes. We list a few of those, based on the impact of our former SDSS-STARLIGHT public database: (a) Stellar population data may be used to complement studies focused on nebular properties. (b) Our catalogue can be used to investigate the host galaxy of transient sources. For instance, if there is a supernova explosion in a CALIFA galaxy ten years from now, interested researchers need simply to look up the corresponding spaxel in our catalogue (Stanishev et al. 2012; Galbany et al. 2014). (c) Finally, other groups might be interested in the stellar population themselves, using our database with a different perspective from our group.

This paper is organised as follows. Section 2 describes the CALIFA observations and the sample selection. In section 3 we discuss how CALIFA galaxies are analysed with STARLIGHT, our spectral synthesis code, and PyCASSO, a tool to organise the synthesis results for IFS data. Section 4 describes the physical and quality control maps available in our value-added catalogue, as well as details on how to access the data. Section 5 shows a few example usages for the catalogue. Some comparisons to data from other sources are presented in Section 6. Our concluding remarks follow in Section 7.

## 2 OBSERVATIONS AND SAMPLE

The survey data was collected using the Potsdam Multi-Aperture Spectrophotometer (Roth et al. 2005, PMAS), in PPAk mode (Kelz et al. 2006). PPAk is a bundle of 382 fibers, each one having  $2.7''$  of diameter. It covers a field of view (FoV) of  $74'' \times 64''$ , with a filling factor of  $\sim 60\%$ .

Observations for CALIFA were obtained in two different spectral settings using the V500 and V1200 gratings. The V500 grating has a spectral resolution of  $\sim 6 \text{ \AA}$  (FWHM), with a wavelength coverage from 3745–7300  $\text{\AA}$ , while the V1200 has a higher spectral resolution of  $\sim 2.3 \text{ \AA}$ , covering the 3650–4840  $\text{\AA}$  range. However, vignetting on the CCD corners reduce the useful wavelength range in some regions of the FoV. The vignetting can be reduced by combining observations using V500 and V1200 gratings. These are called COMBO cubes. A dithering scheme using three observations is used to fill the whole FoV. More information on the observational strategy, effects of vignetting, the reduction pipeline, and data quality can be found in Sánchez et al. (2012) and Sánchez et al. (2016c).

The sample is formed by 445 galaxies of the final CALIFA data release DR3 (Sánchez et al. 2016c) that were observed with both V500 and V1200, and have COMBO cubes. This sample includes 395 galaxies from the main sample, the remaining galaxies are from the extended CALIFA sample. The main sample is a statistically significant subset of the mother sample, which in turn was drawn from the SDSS DR7 (Abazajian et al. 2009). It consists of a representative sample of galaxies of the local universe at the redshift range  $0.005 < z < 0.03$ , with magnitudes ( $-24 < M_r < -17$ ) and colors ( $u - r < 5$ ) that cover all the color magnitude diagram

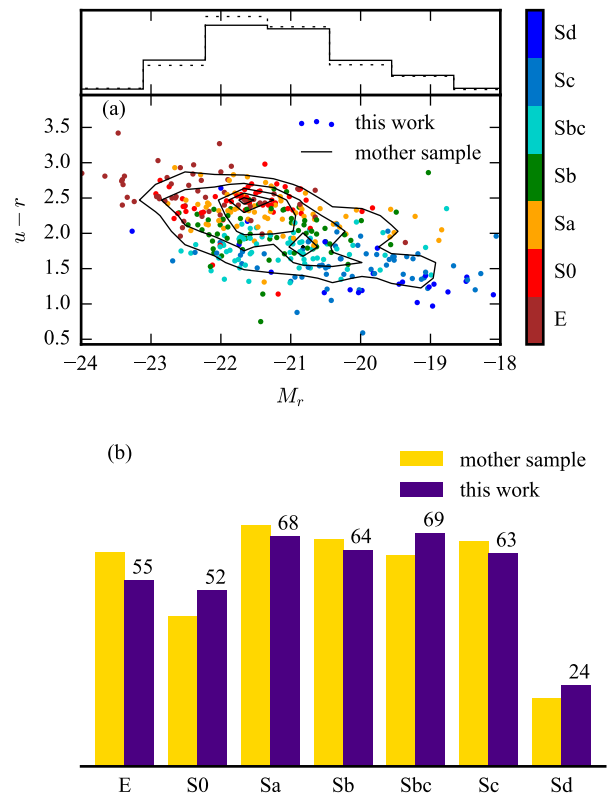


**Figure 1.** Panel (a) Color–magnitude diagram (CMD) of the sample, using photometric magnitudes from SDSS DR7. The black contours show the density of galaxies in the mother sample. The dots, colored by morphological type, show the 395 galaxies with COMBO cubes from the main sample. Above the CMD is the  $M_r$  histogram of both the mother sample, as a black line, and the 395 galaxy sample, as a dotted line. Panel (b) Histogram of morphological types of the mother sample (red bars) and the 395 galaxy sample (blue bars). The histograms are normalized for comparison between the two distributions. The number of galaxies in each type for the 395 galaxies from the main sample is printed above the blue bars.

(CMD). The galaxies were selected by their apparent size with an angular isophotal diameter  $45'' < \text{iso}A_r < 80''$  to fill the FoV of PPAk. A full description of the mother sample is in Walcher et al. (2014). The extended CALIFA sample comes from an heterogeneous set of galaxies observed in different ancillary science projects that are fully described in Sánchez et al. (2016c).

The galaxies from the main and the extended samples were morphologically classified by members of the collaboration through a visual inspection of the SDSS r-band images<sup>2</sup>. Fig. 1a shows the location of the main sample galaxies in the CMD, compared to the mother sample. The distribution by morphological type, again for both samples, is shown in Fig. 1b.

<sup>2</sup> Morphological classification performed by the collaboration is available as ancillary data tables, at the CALIFA DR3 website ([http://www.caha.es/CALIFA/public\\_html/?q=content/dr3-tables](http://www.caha.es/CALIFA/public_html/?q=content/dr3-tables)).

### 3 METHOD OF ANALYSIS

We use a full spectral approach to the stellar population synthesis, using STARLIGHT. The cubes pass through a series of pre-processing steps, meant to extract good quality data for the analysis. These are part of the QBICK pipeline, described in detail in the section 3.2 of Cid Fernandes et al. (2013). The main steps are briefly discussed below.

#### 3.1 Pre-processing

The first step is to mask all spaxels containing light from spurious sources. That includes foreground stars and other galaxies in the FoV. The outer spaxels that have S/N < 3 are also masked.

The cubes are then segmented in Voronoi zones, as implemented by Cappellari & Copin (2003). We use, as input, signal and noise images from the  $5635 \pm 45 \text{ \AA}$  spectral range (the same that is used for spectra normalization, as discussed below). Some modifications were done on the coadded error estimation to account for spatial covariance, as described in the appendix of García-Benito et al. (2015). The target S/N was 20, which lead to most zones inside one half light radius consisting of a single spaxel.

#### 3.2 Spectral synthesis

After the pre-processing steps the resulting spectra are fitted using STARLIGHT (Cid Fernandes et al. 2005). We fit the  $\lambda = 3700$  to  $6850 \text{ \AA}$  rest-frame stellar continuum, masking spectral windows around emission lines ([O II] $\lambda$ 3726/3729, H $\gamma$ , H $\beta$ , [O III] $\lambda$ 5007, He I $\lambda$ 5876, [O I] $\lambda$ 6300, H $\alpha$ , [N II] $\lambda$ 6584, [S II] $\lambda$ 6716/6731). We further mask the Na I doublet at  $\lambda = 5890 \text{ \AA}$  because of possible absorption in the neutral interstellar medium.

The fits decompose the observed spectra in a base built from single stellar populations (SSP). Model SSP spectra are a central ingredient in our analysis, that allow us to link the results of the spectral decomposition to physical properties of the stellar populations. Our previous analysis of CALIFA data (reviewed in section 1) explored different sets of SSP spectra, varying the number of components, the range in metallicity, the specific ages of the SSP, initial mass function (IMF), and stellar evolution. The fits presented here were obtained using two sets of bases, labeled as *GMe* and *CBe*, that have been extensively tested and compared (González Delgado et al. 2015b, González Delgado et al. 2015c, González Delgado et al. 2016). These bases are similar to base *GM* and *CB* of Cid Fernandes et al. (2014), but extended in terms of the metallicity coverage.

Base *GMe* is a combination of 235 SSP spectra from Vazdekis et al. (2010), for populations older than 63 Myr, and González Delgado et al. (2005) models, for younger ages. The evolutionary tracks are those from Girardi et al. (2000), except for the youngest ages (1 and 3 Myr), which are based on the Geneva tracks (Schaller et al. 1992; Schaerer et al. 1993a; Charbonnel et al. 1993; Schaerer et al. 1993b). The metallicity covers the seven bins provided by (Vazdekis et al. 2010):  $\log Z/Z_{\odot} = -2.3, -1.7, -1.3, -0.7, -0.4, 0, +0.22$ , but for SSP younger than 63 Myr, *Z* includes only the the four largest metallicities. The chosen IMF is Salpeter.

Base *CBe* is a combination of 246 SSP spectra provided by Charlot & Bruzual (2007, private communication<sup>3</sup>), covering 41 ages from 0.001 to 14 Gyr, with six metallicities:  $\log Z/Z_{\odot} = -2.3, -1.7, -0.7, -0.4, 0, +0.4$ . The IMF is that from Chabrier (2003). These SSP are an update of the Bruzual & Charlot (2003) models, where STELIB (Le Borgne et al. 2003) is replaced by the MILES (Sánchez-Blázquez et al. 2006) and GRANADA (Martins et al. 2005) spectral libraries. The stellar tracks are those known as “Padova 1994” (Alongi et al. 1993; Bressan et al. 1993; Fagotto et al. 1994a,b,c; Girardi et al. 1996).

Other important issues in our methodology are: a) dust effects are also modeled in the spectral fits as a foreground screen with a Cardelli, Clayton & Mathis (1989) reddening law with  $R_V = 3.1$ ; b) kinematics effects are also taken into account, assuming a Gaussian line-of-sight velocity distribution. Both spectral bases are smoothed to 6 Å FWHM effective resolution prior to the fits. This is because the kinematical filter implemented in STARLIGHT operates in velocity-space, whereas both CALIFA and the SSP spectra have a constant resolution in  $\lambda$ -space. This way the velocity dispersion obtained by STARLIGHT is not contaminated by the spectral resolution mismatch.

#### 3.3 PyCASSO

STARLIGHT was developed to work with individual spectra. The PyCASSO platform was developed to organise its output into spatially resolved data.

The output produced by STARLIGHT is quite large, and it takes a little effort to transform some of the values into familiar physical measurements. PyCASSO takes care of these computations and provides convenient functions that allow us to deal directly with the physical maps. This made the exploration of the data a lot easier, yielding the various results discussed in section 1. These physical maps (and some diagnostic ones) are published in this database, and are described in the following section.

## 4 DESCRIPTION OF THE CATALOGUE

The catalogue is comprised of FITS files containing images for a suite of physical properties of each galaxy of the sample. The files also contain quality control and fit diagnostic maps. A FITS table with properties derived for the integrated spectra of the galaxies is also available. We present these data products below.

#### 4.1 Map data format

Maps are distributed in multi-extension binary FITS files, containing several HDUs. The HDUs consist of a header and an image extension. The headers are all the same for all HDUs, except for the first (primary), which contains additional cards. In particular, CALIFA\_ID and NED\_NAME are present for object identification. BASE informs which SSP base was used in the fit; it may be either *gsd6e* (the *GMe*

<sup>3</sup> The Charlot & Bruzual (2007) models are available at <http://www.bruzual.org/~gbruzual/cb07>.

base) or **zca6e** (the *CBe* base). Also worth mentioning is the luminosity distance used when calculating masses, stored in the card **DL\_MPC**, in units of Mpc. All headers also contain celestial WCS extracted from the original COMBO cubes.

For a given galaxy, the maps are images with the same dimensions. The exact dimensions will change for each galaxy; they are the same as the raw cubes from DR3. Except for **badpix** and **zones**, which are integers, all data are stored as 64-bit floating point numbers. If a pixel is considered “bad” (see Section 4.5.1), its value in all maps is set to zero<sup>4</sup>. The 12 first HDUs, listed in Table 1, contain maps with physical results from STARLIGHT. The remaining 7 HDUs contain data and fit diagnostic maps. The content of these maps are explored in detail in Sections 4.4 and 4.5.

## 4.2 Integrated spectra table data format

We also fit the integrated spectra of the galaxies, summing the flux from all non-masked spaxels. The data are stored in a binary FITS table, with columns described in Table 2. The data are stored as 64-bit floating point numbers, except for **califaID**, which is integer, and **NED\_name** and **base**, which are text strings. The quantities in this table are the same ones provided as maps. Note, however, that the extensive quantities in this table (luminosity, stellar masses, and SFR) are not surface densities.

## 4.3 Data access

The data are publicly available at the PyCASSO web site (<http://pycasso.ufsc.br/>, mirror at <http://pycasso.iaa.es/>). The galaxies are listed with a color SDSS image stamp for reference. There are some preview plots available for each galaxy, in the same fashion as Fig. 2. FITS files with the maps are also available for download, with names following the convention: **KNNNN\_base.fits**. The file names always start with K, and **NNNN** is the CALIFA ID, padded with zeros up to 4 digits. The suffix **base** indicates the base used in the fit, which can be **gsd6e**, for base *GMe*, or **zca6e**, for base *CBe*. For example, the galaxy shown in Fig. 2, fitted using *GMe*, is stored as **K0140\_gsd6e.fits**. Tables with integrated data fitted with both bases are also available for download, with the same suffixes indicating which base.

There is also a form for selecting galaxies based on some of their characteristics. These may be observational (Hubble type, SDSS magnitudes, etc.) or physical quantities obtained on integrated spectra (stellar mass, mean stellar age,  $\tau_V$ , etc.). Given that the dataset is small (445 galaxies  $\times$  2 bases), a simple search form suffices.

The observed data used as input for this work are available at the CALIFA web site (<http://califa.caha.es/DR3/>).

## 4.4 Description of the physical maps

To facilitate the description and illustrate the information content of the catalogue, Fig. 2 shows the maps for a sample

<sup>4</sup> The bad pixels values are set to zero, which may be a valid value depending on the map. A map indicating which pixels are bad is also provided, to help in those cases.

galaxy, CALIFA 0140 (NGC 1667). The SDSS image<sup>5</sup> of this galaxy is shown in panel (a). This is a low inclination Sbc galaxy, with a small bar. It has a half light radius (HLR<sup>6</sup>, computed in the  $5635 \pm 45 \text{ \AA}$  normalization band) of  $15.1''$ , with an ellipticity of  $\epsilon = 0.26$  and position angle of  $177^\circ$ .

In what follows we describe each of the maps available, as well as ways of processing them to improve the results or express them in other forms to highlight certain aspects of the data.

### 4.4.1 Luminosity and stellar mass surface densities

The luminosity surface density ( $\mathcal{L}_{5635\text{\AA}}$ , Fig. 2b) associated to each spaxel is calculated directly from the observed spectra using the median flux in the spectral window of  $5635 \pm 45 \text{ \AA}$ . The map has units of  $L_\odot \text{ \AA}^{-1} \text{ pc}^{-2}$ . The bulge and spiral arms are clearly visible in the image.

The stellar mass surface density ( $\Sigma_\star$ , Fig. 2c) is calculated using the masses derived from STARLIGHT, and are provided in units of  $M_\odot \text{ pc}^{-2}$ . This mass has been corrected for mass that returned to the interstellar medium during stellar evolution, so it reflects the mass currently in stars. The uncorrected mass, i.e., the total mass ever turned into stars,  $\Sigma'_\star$ , is also included in the database.

The morphological structures are still visible in the  $\Sigma_\star$  map. Nonetheless, an artifact is evident in the  $\Sigma_\star$  map: the outer parts of the galaxy are broken in flat patches. This happens because we combine the lower S/N spaxels that are spatially close into Voronoi zones before running STARLIGHT. This behavior occurs in all maps that are products of the synthesis. Only  $\mathcal{L}_{5635\text{\AA}}$ , which comes directly from the spectra, is presented as a full resolution image.

### 4.4.2 Dezonification

Before proceeding with the description of the catalogue maps, it is useful to present a simple data processing to smooth over the spatial effects of the Voronoi zones used in the spectral fitting, as those seen in the image of  $\Sigma_\star$  (Fig. 2c). This procedure was first introduced by Cid Fernandes et al. (2013) to smooth extensive properties, and is generalized below.

The missing information on variations of  $\Sigma_\star$  within the spaxels in a Voronoi zone can be approximately recovered using the  $\mathcal{L}_{5635\text{\AA}}$  image and some mass-to-luminosity relation. We call this procedure “dezonification”. In this paper, we calculate the mean luminosity surface density in each zone, and divide each pixel of the  $\mathcal{L}_{5635\text{\AA}}$  map by this zone average. This yields a map of weights,  $w_{xy}$ . More generally,

<sup>5</sup> SDSS DR13 image obtained from SkyServer.

<sup>6</sup> The half light radius (HLR) is straightforwardly computed by finding the distance where the cumulative sum of the luminosity reaches half of its total value. This is done along the major axis of ellipses with ellipticity and position angle defined by the moments of the image (Stoughton et al. 2002). Note that in this work we calculate HLR using the  $\mathcal{L}_{5635\text{\AA}}$  map, which may or may not have masked regions. Also, in some cases the FoV does not cover the whole galaxy. The HLR is a convenient spatial metric, particularly useful when comparing results obtained for different galaxies.

**Table 1.** Physical quantities and diagnostic maps present in the galaxy cubes.

HDU	Quantity	Units	Extension name	Description
0	$\Sigma_{\star}$	$M_{\odot} \text{pc}^{-2}$	<code>sigma_star</code>	Stellar mass surface density. Mass that is currently trapped inside stars.
1	$\Sigma'_{\star}$	$M_{\odot} \text{pc}^{-2}$	<code>sigma_star_ini</code>	Initial stellar mass surface density. Mass ever formed into stars.
2	$\mathcal{L}_{5635\text{\AA}}$	$L_{\odot} \text{\AA}^{-1} \text{pc}^{-2}$	<code>L_5635</code>	Luminosity surface density in the 5635 Å normalization window.
3	$\langle \log t \rangle_L$	log yr	<code>log_age_flux</code>	Mean log of stellar age, in years, weighted by luminosity.
4	$\langle \log t \rangle_M$	log yr	<code>log_age_mass</code>	Mean log of stellar age, in years, weighted by mass.
5	$\langle \log Z \rangle_L$	log $Z_{\odot}$	<code>log_Z_flux</code>	Mean log of stellar metallicity, in solar units, weighted by luminosity.
6	$\langle \log Z \rangle_M$	log $Z_{\odot}$	<code>log_Z_mass</code>	Mean log of stellar metallicity, in solar units, weighted by mass.
7	$\Sigma_{\text{SFR}}$	$M_{\odot} \text{Gyr}^{-1} \text{pc}^{-2}$	<code>sigma_sfr</code>	Mean star formation rate surface density in the last 32 Myr.
8	$x_Y$	-	<code>x_young</code>	Luminosity fraction of stellar populations younger than 32 Myr.
9	$\tau_V$	-	<code>tau_V</code>	Attenuation coefficient for a dust screen model.
10	$v_{\star}$	$\text{km s}^{-1}$	<code>v_0</code>	Line of sight velocity.
11	$\sigma_{\star}$	$\text{km s}^{-1}$	<code>v_d</code>	Line of sight velocity dispersion.
12	$\bar{\Delta}$	%	<code>adev</code>	Mean model deviation.
13	$N_{\lambda, \text{clip}}/N_{\lambda}$	%	<code>nl_clip</code>	Fraction of the wavelengths clipped by the fitting algorithm.
14	$\chi^2/N_{\lambda}^{\text{eff}}$	-	<code>chi2</code>	Fit statistic.
15	Bad pixels	-	<code>badpix</code>	Masked pixels.
16	Zones	-	<code>zones</code>	Voronoi segmentation zones.
17	S/N	-	<code>sn</code>	Signal-to-noise ratio in individual pixels.
18	S/N (zones)	-	<code>sn_zone</code>	Signal-to-noise ratio in zones.

**Table 2.** Global properties of galaxies using integrated spectra.

Quantity	Units	Column	Description
CALIFA ID	-	<code>califaID</code>	CALIFA galaxy ID.
Object name	-	<code>NED_name</code>	Object name.
Luminosity distance	Mpc	<code>DL_Mpc</code>	Luminosity distance used when calculating stellar masses.
SSP base	-	<code>base</code>	Base used in the fit.
$M_{\star}$	$M_{\odot}$	<code>M_star</code>	Stellar mass currently trapped inside stars.
$M'_{\star}$	$M_{\odot}$	<code>M_star_ini</code>	Total mass ever formed into stars.
$\mathcal{L}_{5635\text{\AA}}$	$L_{\odot} \text{\AA}^{-1}$	<code>L_5635</code>	Luminosity in the 5635 Å normalization window.
$\langle \log t \rangle_L$	log yr	<code>log_age_flux</code>	Mean log of stellar age, in years, weighted by luminosity.
$\langle \log t \rangle_M$	log yr	<code>log_age_mass</code>	Mean log of stellar age, in years, weighted by mass.
$\langle \log Z \rangle_L$	log $Z_{\odot}$	<code>log_Z_flux</code>	Mean log of stellar metallicity, in solar units, weighted by luminosity.
$\langle \log Z \rangle_M$	log $Z_{\odot}$	<code>log_Z_mass</code>	Mean log of stellar metallicity, in solar units, weighted by mass.
SFR	$M_{\odot} \text{Gyr}^{-1}$	<code>sfr</code>	Mean star formation rate in the last 32 Myr.
$x_Y$	-	<code>x_young</code>	Luminosity fraction of stellar populations younger than 32 Myr.
$\tau_V$	-	<code>tau_V</code>	Attenuation coefficient for a dust screen model.
$v_{\star}$	$\text{km s}^{-1}$	<code>v_0</code>	Line of sight velocity.
$\sigma_{\star}$	$\text{km s}^{-1}$	<code>v_d</code>	Line of sight velocity dispersion.
$\chi^2/N_{\lambda}^{\text{eff}}$	-	<code>chi2</code>	Fit statistic.
$\bar{\Delta}$	%	<code>adev</code>	Mean model deviation.
$N_{\lambda, \text{clip}}/N_{\lambda}$	%	<code>nl_clip</code>	Fraction of the wavelengths clipped by the fitting algorithm.

one may compute weights raising the luminosity to some *ad hoc* power  $\alpha$ . That is, for a given zone,

$$w_{xy} = \frac{\mathcal{L}_{xy}^{\alpha}}{N^{-1} \sum_{xy \in z} \mathcal{L}_{xy}^{\alpha}}, \quad (1)$$

where  $x$  and  $y$  are the coordinates of the spaxels inside the zone,  $N$  is the number of spaxels in the zone, and  $\mathcal{L}_{5635\text{\AA}}$  is abbreviated to  $\mathcal{L}$  for clarity. The single  $\Sigma_{\star}$  value for this zone can then be converted to an image through

$$\Sigma_{\star, xy}^{\text{dez}} = w_{xy} \Sigma_{\star}. \quad (2)$$

By design, the total mass of the zones does not change,

we only redistribute the mass among their pixels. Fig. 2f shows an example of dezonification using  $\alpha = 1.4$ . This value was found by fitting  $\Sigma_{\star}$  as a function of  $\mathcal{L}_{5635\text{\AA}}$  for our example galaxy, as seen in Fig. 3a. In Fig. 3b, we show radial profiles of  $\Sigma_{\star}$ , the original (dots and black line) and dezonified versions with various values of  $\alpha$ . Inwards of  $\sim 1.7$  HLR, the curves are identical, because zones there actually correspond to single spaxels ( $N = 1$ ). At larger radii the  $\alpha = 1.4$  line (in green) seems to better represent the cloud of dots for this galaxy, while without dezonification (black line) the profile becomes artificially flatter. Note that the value for  $\alpha$  was calculated for this galaxy only. Other values may be

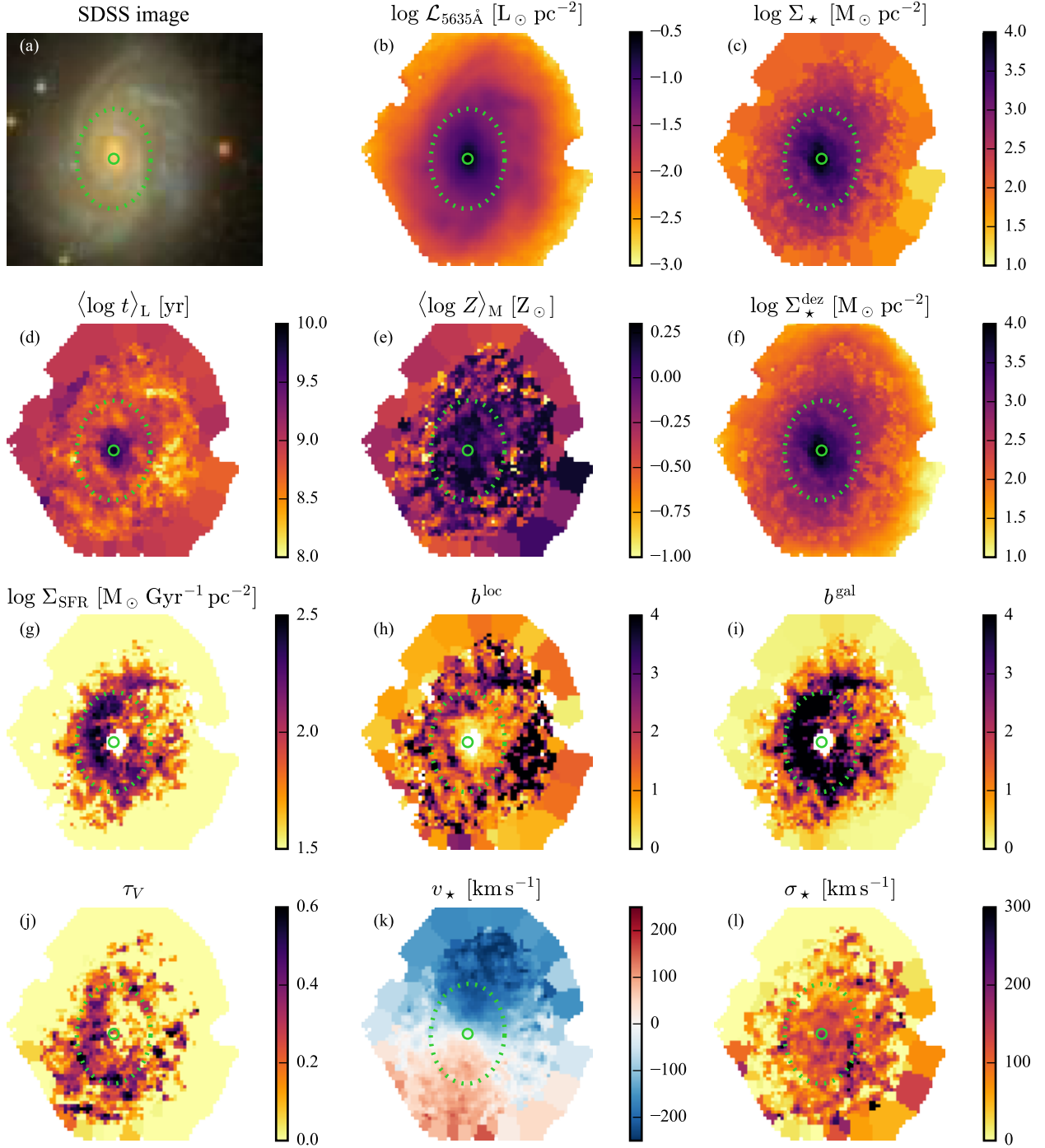


**Figure 2.** Maps with physical properties of CALIFA 0140. A dotted ellipse marks the 1 HLR area, and a small circle marks the galaxy center. See Table 1 for a brief description of each map.

needed for other galaxies, and can be straightforwardly obtained with the data provided in the catalogue. The same overall procedure can be applied to any property that is extensive, that is, scales with the size of the system (for instance,  $\Sigma'_\star$  and  $\Sigma_{\text{SFR}}$ ). Intensive properties, like age and metallicity, are inherently “undezoneifiable”.

#### 4.4.3 Mean stellar age and metallicity

As amply documented in the STARLIGHT-related literature (and indeed for any stellar population synthesis method), the most robust way to summarise the detailed star formation histories retrieved by the spectral fitting is through the

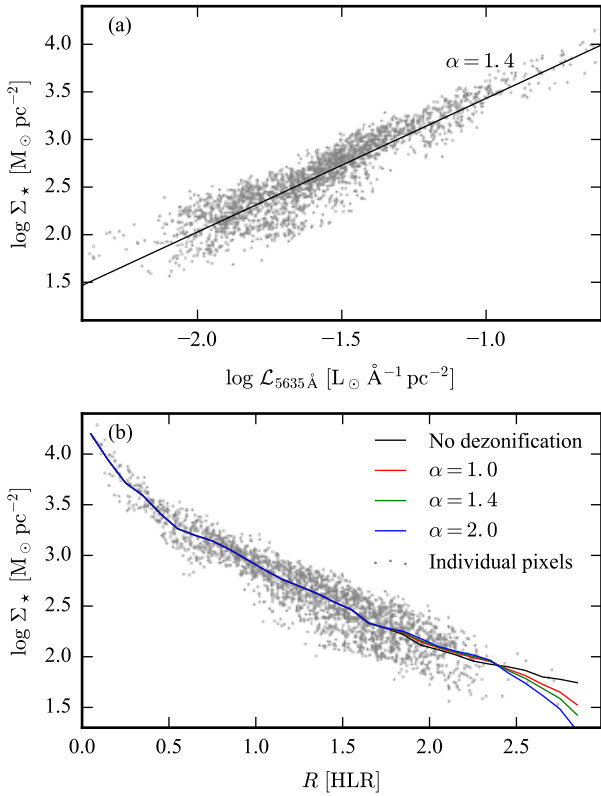


**Figure 3.** Dezonification (see Section 4.4.1) of the mass surface density for CALIFA 0140. *Panel (a)* Mass–luminosity plot to derive the  $\alpha$  parameter used in Equation 1. The black line is the linear fit to the data (gray dots). *Panel (b)* Radial profile of the mass surface density. The dots are the mean mass surface density in each zone. The black line is the mean radial profile without dezonification, while the colored lines are the profiles with dezonification for different  $\alpha$  values. The value used in this work is  $\alpha = 1.4$  (green).

first moments of the age and metallicity distributions. We present the mean stellar age (in years) and metallicity (in solar units), both weighted by luminosity and mass, defined as follows:

$$\langle \log t \rangle_L = \sum_j x_j \log t_j \quad (3)$$

$$\langle \log t \rangle_M = \sum_j \mu_j \log t_j \quad (4)$$

$$\langle \log Z \rangle_L = \sum_j x_j \log Z_j \quad (5)$$

$$\langle \log Z \rangle_M = \sum_j \mu_j \log Z_j \quad (6)$$

The luminosity weighted mean stellar age (Equation 3) and mass weighted mean stellar metallicity (Equation 6) are shown in panels (d) and (e) of Fig. 2. Most of the works on stellar population use these two definitions. Stellar metallicity is directly related to the mass, which justifies this choice.

On the other hand, the mean age spans a larger dynamical range weighting by light, which helps better mapping younger populations. A spiral pattern is present in both maps, following the spiral seen in luminosity. Negative gradients are present in both age and metallicity. These become more evident with a little processing of the data, as seen in Section 5.1.

These are all intensive quantities, independent of the size of the system. Thus, unlike  $\Sigma_\star$  and  $\Sigma_{\text{SFR}}$ , they are intrinsically not dezonifiable.

#### 4.4.4 Star formation rate surface density

Fig. 2g shows the map of the mean recent star formation rate surface density<sup>7</sup> ( $\Sigma_{\text{SFR}}$ ), obtained by adding the mass turned into stars in the last  $t_{\text{SF}} = 32$  Myr and dividing by this time scale (Asari et al. 2007; Cid Fernandes et al. 2015). The maps are in units of  $M_\odot \text{Gyr}^{-1} \text{pc}^{-2}$ . Close to the spiral arms we see higher values of  $\Sigma_{\text{SFR}}$ .

Unlike for the mass and luminosity densities, this map has some empty patches. To remove possible spurious young populations (intrinsic to the way STARLIGHT works), we mask the zones where the fraction of luminosity in populations younger than 32 Myr, that is, the  $x_Y$  map, is smaller than 3% (see González Delgado et al. 2016 for details). Dezonification of this map is also possible, but there is a caveat. The luminosity map represents the median luminosity in the  $5635 \pm 45 \text{ \AA}$  band, a wavelength which is not usually dominated by the  $t < t_{\text{SF}}$  populations which go into the computation of  $\Sigma_{\text{SFR}}$ . Users may thus prefer to use the image at a shorter wavelength (extractable from the raw DR3 data) to obtain more suitable dezonification weights.

It may be useful to consider  $\Sigma_{\text{SFR}}$  in relation to some fiducial value instead of absolute units. Cid Fernandes et al. (2013) uses Scalo’s birthrate parameter  $b$  as an example, which measures the SFR in recent past ( $t < t_{\text{SF}}$ ) with respect to the average over the entire lifetime of the system. The latter is actually  $\Sigma_\star$  divided by the age of the oldest population in the base,  $t_\infty = 14.1$  Gyr. The birthrate parameter may be straightforwardly computed from the  $\Sigma'_\star$  and  $\Sigma_{\text{SFR}}$  maps distributed in our database:

$$b = \frac{\langle \Sigma_{\text{SFR}} \rangle (t_{\text{SF}})}{\langle \Sigma_{\text{SFR}} \rangle (t_\infty)} = \Sigma_{\text{SFR}} \frac{t_\infty}{\Sigma'_\star}. \quad (7)$$

The reference SFR value does not need to be local. For example, we define two  $b$  parameters, one where the reference value is the mean SFR surface density of the same spaxel ( $b^{\text{loc}}$ ), and another where the reference value is the mean SFR surface density of the whole galaxy ( $b^{\text{gal}}$ ). These maps are shown in Figs. 2h and 2i.  $b^{\text{loc}}$  shows regions where the star formation is currently stronger locally, independent of the total mass formed, while  $b^{\text{gal}}$  shows where in the galaxy the current SFR is stronger. Note that the  $b^{\text{gal}}$  map is equivalent to that in Fig. 2d, but in different units and in a linear scale. These maps are shown here as examples of simple operations over the data distributed in our catalogue to highlight one or another aspect of interest.

<sup>7</sup> Also known as star formation rate intensity in some works.



#### 4.4.5 Attenuation coefficient

STARLIGHT models the dust attenuation with a foreground screen factor, that is

$$F_{\lambda}^{\text{obs}} = F_{\lambda}^{\text{int}} \exp(-\tau_{\nu} q_{\lambda}), \quad (8)$$

where  $F_{\lambda}^{\text{int}}$  is intrinsic flux behind the dust screen, and  $F_{\lambda}^{\text{obs}}$  is the resulting observed flux. Fig. 2j shows the map of the V-band optical depth  $\tau_{\nu}$  obtained for CALIFA 0140. The values range from 0 to 0.6, with an overall average of 0.1. The morphology of the  $\tau_{\nu}$  maps roughly follows that of the recent SFR (panels d and f), which fits with the notion that star-forming regions are dustier than the general interstellar medium.

As in the case of mean ages and metallicities, the  $\tau_{\nu}$  maps are not dezonifiable. One could, in principle, modify our dezonification scheme by defining weights in terms of colors instead of fluxes, and attribute larger  $\tau_{\nu}$  values to the redder spaxels within a zone according to an empirically calibrated relation analogous to that in Fig. 3a. Known degeneracies with other stellar population properties (mainly age) complicate this extension of the dezonification method, but it might still be worth exploring this possibility.

#### 4.4.6 Stellar kinematics

Stellar velocity ( $v_{\star}$ ) and velocity dispersion ( $\sigma_{\star}$ ) maps are shown in Figs. 2k and l, respectively. Again, dezonification is not possible with these images.

The rotation pattern is clearly seen in the  $v_{\star}$  map, with projected speeds reaching  $\sim 200 \text{ km s}^{-1}$ . The  $\sigma_{\star}$  map shows a decline towards the outside. There are, however, several low  $\sigma_{\star}$  patches, as well as some high  $\sigma_{\star}$  spikes, none of which seem real.

These artifacts are a consequence of the low resolution (FWHM = 6 Å) of the spectra, as well as of intrinsic difficulties faced by STARLIGHT in fitting  $\sigma_{\star}$  under some circumstances (like noisy spectra or dominant young populations). We thus recommend caution in the use of the  $\sigma_{\star}$  maps provided in the catalogue. A much more precise kinematical analysis is possible with the V1200 grism (FWHM = 2.7 Å) datacubes, not analysed here because their limited wavelength coverage makes them less informative for a stellar population analysis. Falcón-Barroso et al. (2017) have recently published<sup>8</sup> a detailed kinematical analysis of 300 CALIFA galaxies using this higher resolution setup.

### 4.5 Quality-control and uncertainties

Despite the homogeneity of CALIFA data, there are relevant variations in data quality both within and between galaxies. Moreover, the STARLIGHT fits themselves can be bad even in cases the data are good, e.g., because of unmasked strong emission lines. It is thus important to keep track of these caveats in order to evaluate to which extent they affect the results of any one particular analysis.

Our catalogue offers a suite of indices to carry out this

<sup>8</sup> Stellar kinematics maps from Falcón-Barroso et al. (2017) are available at [http://www.caha.es/CALIFA/public\\_html/?q=content/science-dataproducts](http://www.caha.es/CALIFA/public_html/?q=content/science-dataproducts).

quality control. The indices are listed in rows 12–18 of Table 1. Quality control maps for CALIFA 0140 are shown as an example in Fig. 4 and discussed in sections 4.5.1 and 4.5.2 below. A discussion of the uncertainties in the derived properties is also presented (section 4.5.3).

#### 4.5.1 Data quality maps

Before running the spectra through STARLIGHT, some pre-processing is necessary. The most basic is flagging spaxels that we do not want to apply the synthesis to. That includes spaxels with artifacts, foreground objects, and very low S/N spaxels ( $< 3$ ). These become masked regions in the maps, where there is no data, appearing white in Figs. 2 and 4. The mask is stored in the Bad pixel map.

As discussed in Section 3.1, and detailed in section 3.2 of Cid Fernandes et al. (2013), the spaxels with S/N lower than 20 are then binned into Voronoi zones. The zones map assigns a zone number to each pixel, so that if two or more pixels are contained in a given zone, then they share the same number.

Fig. 4a shows the area of the Voronoi zones for our example galaxy. As expected, the outer parts of the galaxy have larger zones. The black contour indicates the region where the zones are composed of a single pixel, reaching approximately 2 HLR of the galaxy in this case. This map may be used, for example, to calculate the total mass in each zone. It is also used in the dezonification procedure explained in Section 4.4.2.

Fig. 4b shows the pixel-by-pixel S/N ratio in the  $5635 \pm 45 \text{ \AA}$  band. The outer parts of the galaxy have S/N well below 10. With the Voronoi binning all the spectra have S/N  $> 20$ , as can be seen in Fig. 4c.

#### 4.5.2 Fit quality maps

Even if the spectra were classified as good by the previous criteria, we must assert that the fit was successful. Fig. 4d shows the map of the fit quality indicator  $\bar{\Delta}$ , defined as

$$\bar{\Delta} = \frac{1}{N_{\lambda}^{\text{eff}}} \sum_{\lambda} \frac{|O_{\lambda} - M_{\lambda}|}{M_{\lambda}}, \quad (9)$$

where  $N_{\lambda}^{\text{eff}}$  is the number of wavelengths effectively used in the fit, and  $O_{\lambda}$  and  $M_{\lambda}$  are the observed and model spectra, respectively. The figure of merit actually used by STARLIGHT is  $\chi^2$ , which is shown in Fig. 4e divided by  $N_{\lambda}^{\text{eff}}$ .

Usually, one would resort to  $\chi^2$  to check the quality of the fit. However,  $\chi^2$  is closely tied to the uncertainty of the spectra ( $\epsilon_{\lambda}$ ), which is sometimes difficult to estimate precisely. Due to the clipping algorithm, discussed below, the number of measurements effectively used in the fit ( $N_{\lambda}^{\text{eff}}$ ) varies between the spaxels. Therefore we use  $\chi^2/N_{\lambda}^{\text{eff}}$  to be able to compare the fit statistic between them. Inspection of Fig. 4e may lead to the wrong conclusion that the spectral fits are worse in the nuclear regions than outside, but the larger  $\chi^2/N_{\lambda}^{\text{eff}}$  values in those regions is because of smaller errors (larger S/N, as seen in panel c), not worse fits. The mean absolute deviation  $\bar{\Delta}$  does not depend explicitly on the uncertainties, so its map in Fig. 4a conveys a more appropriate measure of the fit quality.

Another useful quantity to keep track of is the amount

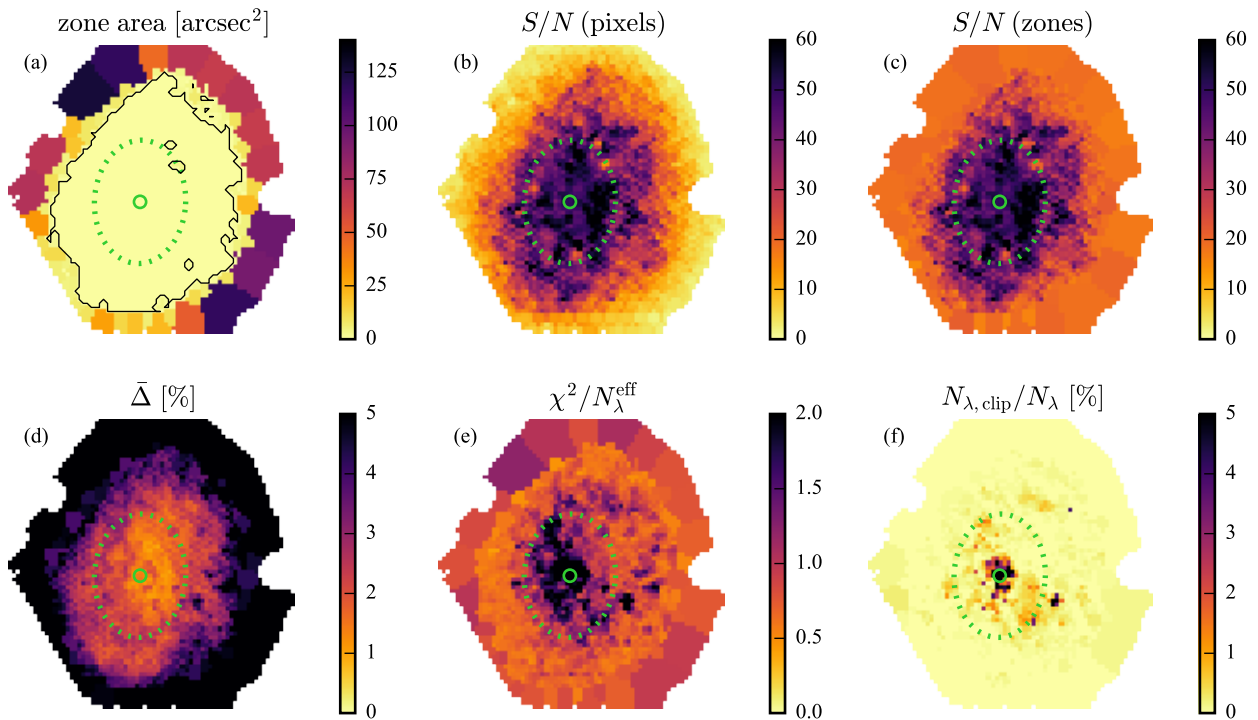


**Figure 4.** Maps with fit quality indicators of NGC 1667 (CALIFA 0140). A dotted ellipse marks the 1 HLR area, and a small circle marks the galaxy center. See Table 1 for a brief description of each map.

of clipping done by STARLIGHT during the fit. If some wavelengths have fluxes that are outliers, over  $\pm 4\epsilon_\lambda$  off the model during the fit, they are flagged as clipped, and not used in the fit anymore. This is enforced to keep artifacts and non-masked emission lines from messing up the fit. The fraction of clipped wavelengths, given by  $N_{\lambda,\text{clip}}/N_\lambda$ , is shown in Fig. 4f. For CALIFA 0140, the median fraction of clipping is 3.5%, with very few going over 5%. Nevertheless, given that these are usually only a handful among the thousands of pixels, they are usually irrelevant for statistics that take large slices of the maps.

#### 4.5.3 Uncertainties

STARLIGHT does not provide error estimates in its output. These uncertainties are usually explored by perturbing the data according to some prescription related to observational and calibration errors, and performing the spectral synthesis several times (e.g., Cid Fernandes et al. 2005).

It is not practical, in our case, to run the synthesis code dozens of times for all spectra from CALIFA. We can, however make use of the simulations by Cid Fernandes et al. (2014) to estimate the uncertainties associated to the physical properties obtained by STARLIGHT. The simulations were performed using data from a single galaxy, CALIFA 0277. The spectra were perturbed in different ways to estimate the effects of noise, calibration issues and multiplicity of solutions.

Table 3 lists estimated uncertainties associated to the maps in our catalogue. These values are based on the OR1 simulations in Cid Fernandes et al. (2014), in which Gaus-

**Table 3.** Estimated uncertainties of physical quantities, obtained by simulations (Cid Fernandes et al. 2014).

Quantity	Uncertainty	
	$20 < S/N < 30$	$40 < S/N < 50$
$\log M_\star$	0.09	0.04
$\langle \log t \rangle_L$	0.08	0.05
$\langle \log t \rangle_M$	0.15	0.07
$\langle \log Z \rangle_L$	0.08	0.05
$\langle \log Z \rangle_M$	0.12	0.07
$\log \text{SFR}$	0.16	0.14
$x_\gamma$	0.03	0.01
$\tau_V$	0.05	0.02
$v_\star$ [km s $^{-1}$ ]	19	9
$\sigma_\star$ [km s $^{-1}$ ]	22	10

sian noise with amplitude given by the error in fluxes was injected in the data. The uncertainties are obtained by taking the standard deviation of the difference between the results from perturbed and original spectra. Except for  $x_\gamma$ ,  $v_\star$  and  $\sigma_\star$ , the uncertainties are logarithmic, independent of scale. That means the uncertainties in  $\log \Sigma_\star$  and in  $\log \Sigma'_\star$  are the same as the uncertainties for  $\log M_\star$  given in the table.

Table 3 complements and expands upon a similar table presented in Cid Fernandes et al. (2014). While in that paper the uncertainties were evaluated considering all zones of the galaxy, here we break them into two bins in S/N, one for zones where  $20 < S/N < 30$ , and another one for  $40 < S/N < 50$ , which roughly translates to outer and inner regions of

galaxies, respectively (see Fig. 4c for an example). We find that uncertainties decrease by typically a factor of two from the high to the low S/N bin. Uncertainties for individual zones may be obtained by interpolating the values given in Table 3, and using the S/N diagnostic maps. Naturally, these uncertainty estimates must be interpreted as approximate, as they are based on experiments with a single galaxy, and do not take into consideration sources of error other than random noise (like the continuum calibration, also explored by Cid Fernandes et al. 2014).

An independent and more empirical estimate of the uncertainties may be obtained from the catalogue data itself, by comparing regions known to have similar spectra, as those along fixed radial bins in elliptical galaxies, or in the bulges of spirals. This recipe is explored in Section 5.1.1 for CALIFA 0140.

#### 4.6 Integrated spectral analysis

We now turn to the properties derived from the integrated spectra in our catalogue (i.e. simulating a single-beam observation for each galaxy). In the following, we compare physical properties obtained directly from the integrated spectra to the same properties obtained by integrating the spatially resolved results. Since there is only one integrated spectrum per object, we must thus set aside the analysis of one single sample galaxy and consider all galaxies in our main sample.

Fig. 5a shows that the total stellar mass  $M_\star$  obtained from the integrated spectra and integrated spatially resolved masses agree remarkably well.

For intensive properties, the way to reach a global value will vary according to the nature of the property. Average ages and metallicities must be weighted by luminosity or mass. For instance, taking into consideration Equation 3, we may calculate the average stellar age of the whole galaxy (in fact, for any set of pixels), weighted by luminosity, using

$$\langle \log t \rangle_L^{\text{gal}} = \frac{\sum_{x,y} \mathcal{L}_{xy} \langle \log t \rangle_{L,xy}}{\sum_{x,y} \mathcal{L}_{xy}}, \quad (10)$$

where  $\mathcal{L}_{xy}$  and  $\langle \log t \rangle_{L,xy}$  are the maps for  $\mathcal{L}_{5635\text{\AA}}$  and  $\langle \log t \rangle_L$ , respectively. The weight for mass weighted quantities is  $\Sigma_{\star,xy}$ . The same equation applies to stellar metallicity. Figs. 5b and 5c shows the comparison between the integrated and mean of the maps for  $\langle \log t \rangle_L$  and  $\langle \log Z \rangle_M$ , respectively. There is a fairly good agreement of both measurements for mean stellar age, with a bit more scatter than the plot for stellar mass. The results for metallicity are similar, but with more scatter.

In the lower panels of Fig. 5 we present a comparison between the mean values over the whole galaxy to the mean over a ring at  $1 \pm 0.1$  HLR from the nucleus. The plots show that, for stellar ages and metallicities, the value at 1 HLR is a good proxy for the mean of the whole galaxy. The same is not strictly valid for  $\Sigma_\star$  (Fig. 5). This happens because the mean stellar mass surface density of a galaxy is not a well defined value. Given that  $\Sigma_\star$  decreases with the radius, depending on which radius is chosen as the ‘‘boundary’’ of the galaxy, the surface density can become arbitrarily small. The galaxies of the sample were observed typically up to  $\sim 2.5$  HLR. Calculating the average over 2 HLR, for example,

moves the points closer to the diagonal. These results confirm what was obtained by González Delgado et al. (2014a), who used the first 107 galaxies observed by CALIFA to perform this same kind of integrated versus resolved analysis.

#### 4.7 Comparison of results with different bases

All examples presented in this paper were obtained with base *GMe*, described in Section 3.2. As mentioned there, our catalogue also offers results derived with *CBe*. Previous papers in this series combining CALIFA data with a STARLIGHT analysis have compared results obtained with these two bases, drawn from independent sets of evolutionary synthesis models (Cid Fernandes et al. 2014; González Delgado et al. 2015c, 2016). In the interest of completeness, and also to update these previous comparisons to our final sample, Fig. 6 compares properties derived with these two bases, for all 395 galaxies of the main sample. These properties were averaged in radial bins up to 2.5 HLR, in steps of 0.1 HLR. See Section 5.1.1 for more details on radial profiles. The averaging strategy for intensive quantities is the same adopted in the previous section, using Equation 10.

Panels a–d of Fig. 6 compare the intensive properties  $\langle \log t \rangle_L$  (panel a),  $\langle \log Z \rangle_M$  (b),  $\tau_V$  (c), and the fraction of light in stellar populations younger than 32 Myr ( $x_Y$ , d) obtained with bases *GMe* (horizontal axis) and *CBe* (vertical axis). The other panels compare the results for  $\Sigma_\star$  (panel e), and  $\Sigma_{\text{SFR}}$  (f), both of which are extensive and IMF-sensitive quantities. In all panels the mean ( $\bar{\Delta}$ ) and standard deviation ( $\sigma_\Delta$ ) of the  $\Delta \equiv y - x = \text{CBe} - \text{GMe}$  difference are indicated.

The results in Fig. 6 agree with our previous comparisons for smaller samples. Mean stellar ages using *CBe* are 0.16 dex lower, on average. As indicated by the tendency of the offset to increase towards smaller values of  $\langle \log t \rangle_L$  in panel a, the difference is mostly due to the fact that young stellar populations come out somewhat stronger with *CBe* than with *GMe*, as confirmed in panel d. Metallicities are somewhat larger when using *CBe* because its base models reach higher  $Z$  than *GMe*, while the dust attenuation is essentially the same ( $\bar{\Delta}\tau_V = 0.02$ ). The stellar mass surface density is lower by a factor of  $\sim 2$  when using *CBe*, reflecting the different IMF used in each base. Differences in  $\Sigma_{\text{SFR}}$  values, however, are not as large, with an offset of only 0.06 dex. As seen above in the  $x_Y$  comparison, the fraction of mass in young stellar populations is higher with *CBe*, which compensates for the lower absolute mass due to differences between the Chabrier and Salpeter IMFs.

Despite the non-negligible differences between bases *CBe* and *GMe*, the general results are essentially the same. There are, naturally, systematic offsets in the properties derived with these two sets of models, but these are ultimately not relevant in a comparative analysis, which is essentially what one aims when studying spatial variations of properties such as mean stellar age, metallicity, or attenuation caused by dust.

## 5 USING THE CATALOGUE

The data in our PyCASSO database can be used in a variety of ways to address a wide ranging spectrum of questions.

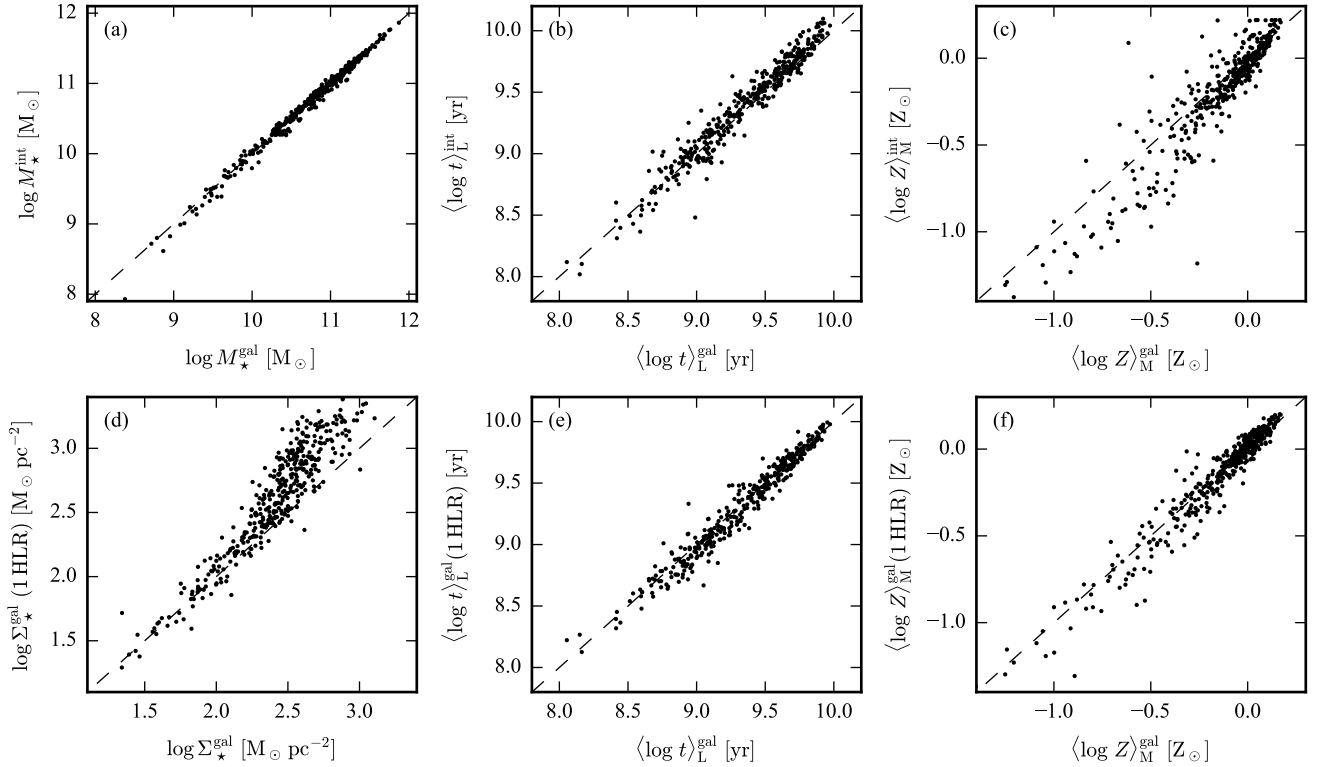


**Figure 5.** Properties from integrated spectra (superscript “int”) versus spatially resolved properties (superscript “gal”) for all galaxies in the sample. *Panel (a)* Mass obtained from the integrated spectra against the total mass in the integral of mass surface density map. *Panel (b)* Luminosity-weighted stellar age from the integrated spectra against the mean of stellar ages of all pixels. *Panel (c)* The same as panel (b), but for mass-weighted stellar metallicity. *Panel (d)* Mean stellar mass surface density of the whole galaxies against the mean in a ring of 1 HLR around the galaxy nucleus. *Panel (e)* The same as panel (d), but for luminosity-weighted stellar age. *Panel (f)* The same as panel (d), but for mass-weighted stellar Metallicity. The dashed lines show the  $y = x$  diagonal.

This section gives concrete examples of the kind of work that can be carried out with some simple processing of the maps made publicly available, as described in Section 4.3.

An underlying characteristic of all examples below is that they explore the statistical power of the database, be it using all 316,960 zones in all 395 galaxies from the main sample, in subsamples focusing on certain types of galaxies, or even in single galaxies, which become statistical samples themselves with IFS data. This is not only a sensible approach, but a firmly established working philosophy within the stellar population synthesis community, which, acknowledging the several uncertainties involved in properties retrieved from single spectra, has long vouched for a statistical approach (Panter et al. 2007; Cid Fernandes et al. 2013).

Examples of how to use our database for single galaxies are explored in Section 5.1, while Section 5.2 presents examples of what can be done for samples of galaxies. As anticipated in the introduction (and as already done in Fig. 5), we take the opportunity to update some of the results obtained in our own earlier work.

## 5.1 Examples of usage for a single galaxy

Maps such as those in Fig. 2 are good for a global appreciation of the results and locating particular spots of the

galaxies, like HII regions or spiral arms, but they are not convenient to visualise trends and gradients. By reducing the dimensionality of the data we may have a better grasp of the behaviour of the physical properties. With radial profiles, we take advantage of both statistics and visualisation.

### 5.1.1 Radial profiles

As an example, Fig. 7 shows radial profiles for some of the physical properties for CALIFA 0140. Each plot shows the values of some property for each zone as gray dots, while the average and  $\pm$  one sigma dispersion in radial bins are shown by the thick and thin solid lines. The radial bins are elliptical annuli with thickness of 0.1 HLR. A vertical dashed line marks the HLR for this galaxy. We warn that this simple statistics may not be the wiser way to treat the physical quantities in this plot, but it suffices for our current illustrative purposes.

Panels a–d show the radial run of  $\langle \log t \rangle_L$ ,  $\langle \log Z \rangle_M$ ,  $\Sigma_{\text{SFR}}$ , and  $\tau_V$ , respectively. The estimated uncertainties, described in Section 4.5.3 are shown as single errorbars in each panel. There is substantial scatter in the plots, but the mean radial profiles are well behaved. The mean stellar age ( $\langle \log t \rangle_L$ , Fig. 7a shows a clear drop from the center down to  $R \sim 0.7\text{HLR}$ , where it levels off at a value of about

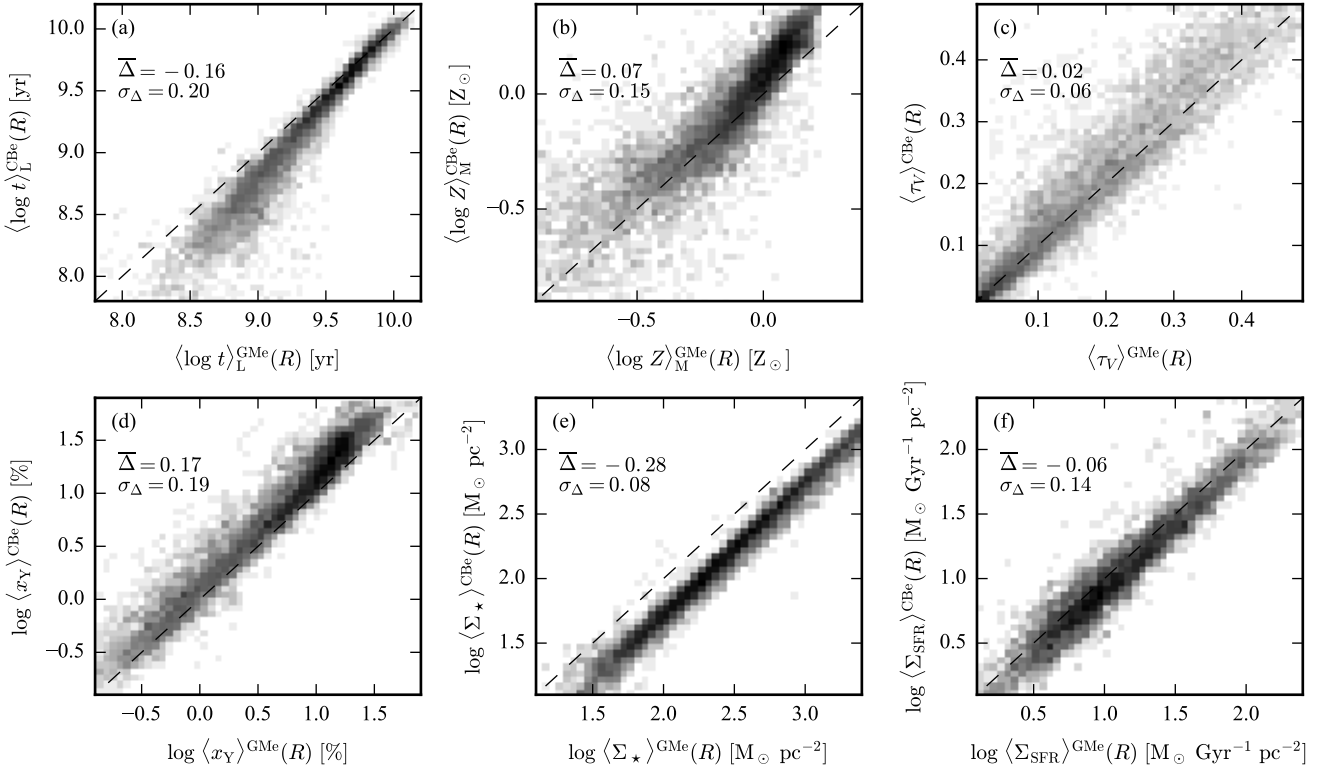


**Figure 6.** Comparison between the synthesis results using bases *GMe* and *CBe*. The panels show 2D histograms of values averaged in radial bins of all 395 maps of the main sample. The horizontal and vertical axes are values obtained using *GMe* and *CBe*, respectively. In each panel we also show the mean and standard deviation of the difference between *CBe* and *GMe*. (a) Luminosity weighted mean stellar age. (b) Mass weighted mean stellar metallicity. (c) Dust attenuation. (e) Fraction of light in populations younger than 32 Myr. (e) Stellar mass surface density. (f) Star formation rate surface density.

0.5 Gyr. The mass weighted mean stellar metallicity  $\langle \log Z \rangle_M$  decreases more or less steadily by  $\sim 0.4$  dex from the nucleus to the outskirts of the galaxy (Fig. 7b). The large scatter is not surprising considering that metallicities are notoriously harder to estimate than ages. The  $\Sigma_{\text{SFR}}$  profile (Fig. 7c) peaks at about 0.7HLR, coinciding with the inflection in the  $\langle \log t \rangle_L$  profile, decreasing both towards the inner bulge region and the outer disk, as indeed seen (but less clearly so) in the full  $\Sigma_{\text{SFR}}$  maps in Fig. 2g. The dust optical depth<sup>9</sup> shows weaker trends, slowly decreasing towards 0 outwards of  $\sim 1$  HLR (more or less in tandem with the  $\Sigma_{\text{SFR}}$  profile), and slowly decreasing to values around 0.2 in the nucleus.

As anticipated in section 4.5.3, these profiles may be used to estimate the uncertainties adopted for the properties. For CALIFA 0140 the region inside 0.7HLR is the bulge of the galaxy. Given that the bulge is fairly symmetrical, the spectra in a radial bin will be roughly equivalent to multiple observations of the same object. This means that the disper-

sion of the radial profiles serve as an empirical estimate of the uncertainty of these properties. In fact, as the error-bars in Fig. 7 illustrate, they are in good agreement with the estimated uncertainties obtained by simulation (Cid Fernandes et al. 2014), presented in Table 3.

The argument of symmetry does not apply to the outer parts of this particular galaxy. The spiral pattern breaks the symmetry, which means the dispersion in the profiles increases outside of 0.7HLR, is caused by the data. Nevertheless it is still a good estimator of the uncertainty for, e.g., asserting that a gradient in a radial profile is significant.

Further analysis may be done by combining the values present in the catalogue maps. For instance, in Fig. 7e we show  $\tau_V/\Sigma_\star$  to obtain a proxy for the dust-to-stars ratio (itself a proxy for the gas-to-stars ratio given some hypothesis about dust/gas). As shown in González Delgado et al. (2014a),  $\tau_V$  profiles generally tend to show negative gradients, which one might read as a tendency for galaxies to be less dusty towards their outer regions. Fig. 7e conveys a different impression, however. The rise of  $\tau_V/\Sigma_\star$  with radius indicates that here are more dust particles per star as one moves away from the nucleus, a trend which may ultimately be reflecting the fact that galaxies are more gas rich towards the outside.

<sup>9</sup> Note that STARLIGHT assumes a dust screen and finds the *effective* attenuation at each zone of a CALIFA galaxy. Thus one should be careful when interpreting  $\tau_V$  as the dust optical depth. In addition, the arithmetic averaging of  $\tau_V$  may be misleading: the radial profiles show the typical value of  $\tau_V$  at a given radius, but not the effective attenuation one would obtain if analysing the coadded spectra in a ring.

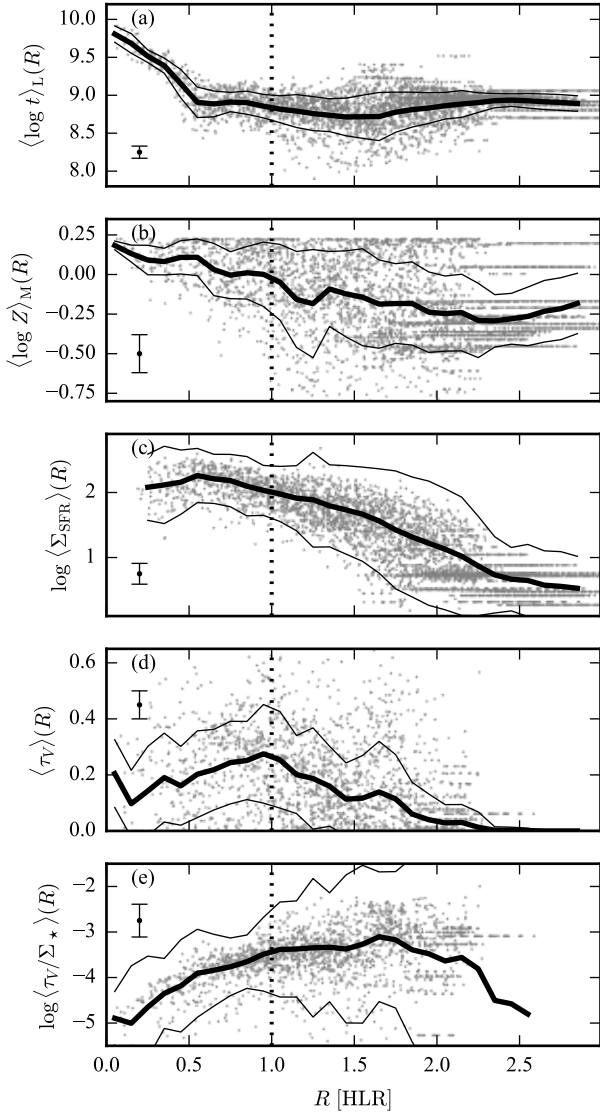


**Figure 7.** Radial profiles of some physical quantities for CALIFA 0140. The gray dots are the values for individual pixels. The black lines are the mean values in radial bins of width 0.1 HLR, with the  $1\sigma$  range shown by thin black lines. The vertical dotted line marks 1 HLR. Typical uncertainties associated to these quantities (with the lowest S/N from Table 3) are shown as single error-bars at the left side of the plots. See Table 1 for a brief description of these quantities. From top to bottom: luminosity-weighted mean stellar age (a), in [yr]; mass-weighted mean stellar metallicity (b), in  $[Z_\odot]$ ; star formation rate surface density (c), in  $[M_\odot \text{Gyr}^{-1} \text{pc}^{-2}]$ ; dust attenuation (d), dimensionless; dust-to-stars ratio (e), in arbitrary units.

### 5.1.2 Bulge-disk decomposition in light and mass

Perhaps the most traditional type of surface photometry analysis for spirals is bulge/disk decomposition (Kormendy 1977; Kent 1985). The data distributed in our catalogue allow one to perform this kind of analysis both in light ( $\mathcal{L}_{5635\text{\AA}}$ ) and mass ( $\Sigma_\star$ ) surface densities.

A morphological analysis of our  $\mathcal{L}_{5635\text{\AA}}$  images (or those produced at any other  $\lambda$ ) is not particularly attractive *per se*,

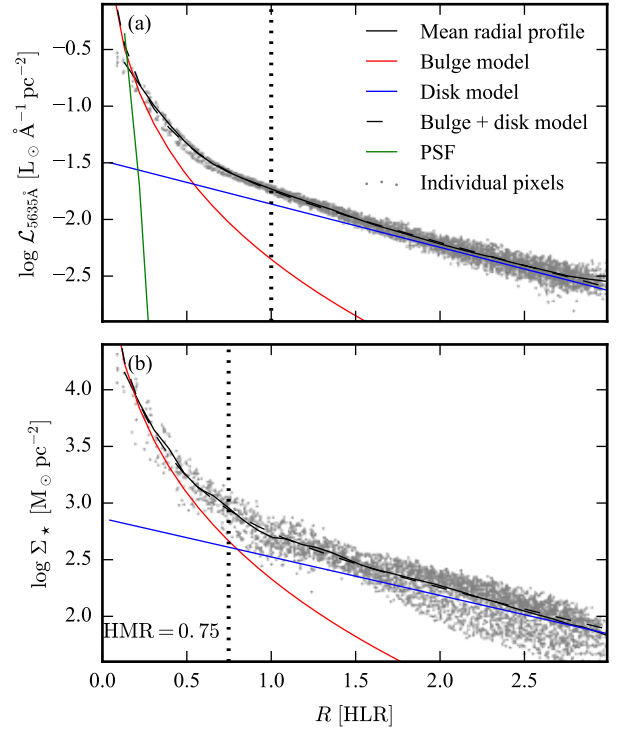


**Figure 8.** Bulge/disk fit of luminosity (a) and mass (b) surface densities for CALIFA 0127. The morphology models (Equations 12 and 11) were fitted to radial profiles of these properties. The central  $2.5''$  were masked to avoid issues with PSF convolution (the green line shows the PSF profile). The vertical dotted line marks 1 HLR in panel (a) and 1 HMR in panel (b). Blue and red lines in both panels show respectively the fitted disk and bulge models, while a dashed black line shows the combined models.

as the image quality of CALIFA is inferior that of publicly available photometry. Indeed, Méndez-Abreu et al. (2017) have recently used SDSS images to perform a morphological analysis of CALIFA galaxies. The mass density maps, however, are clearly of interest, despite the limitations in resolution. Bulge and disk parameters deduced from an analysis of  $\Sigma_\star$  images are not only more physically meaningful, but also less ambiguous than those derived from the surface brightness, which have the inconvenient property of depending on the wavelength of the image.

Fig. 8 shows the radial profiles of  $\mathcal{L}_{5635\text{\AA}}$  (top) and  $\Sigma_\star$  (bottom) for the S0 galaxy CALIFA 127 (NGC 1349). The stellar mass density image is dezonified using  $\alpha = 1.2$ , following the prescription outlined in Section 4.4.2. Maps of physical properties for this galaxy are shown in the appendix. Values for individual spaxels are shown as dots, while the solid black line shows the azimuthally averaged profiles. Red and blue lines show the results of a simplified bulge (red) + disk (blue) decomposition applied to these 1D profiles. The bulge was modeled as following a classical de Vaucouleurs  $R^{1/4}$  profile:

$$I_B(R) = I_e \exp \left\{ -7.669 \left[ \left( \frac{R}{R_e} \right)^{1/4} - 1 \right] \right\}, \quad (11)$$

while the disk was modeled as

$$I_{\text{D}}(R) = I_0 \exp\left(-\frac{R}{h}\right). \quad (12)$$

The parameters in these expressions have their usual meaning:  $R_e$  is the bulge effective radius,  $I_e$  is the intensity at  $R = R_e$ ,  $h$  is the disk scale radius, and  $I_0$  the central intensity of the disk component. The total profile is simply  $I(R) = I_{\text{B}}(R) + I_{\text{D}}(R)$ . The intensity  $I$  refers to  $\mathcal{L}_{5635\text{\AA}}$  in Fig. 8a and to  $\Sigma_{\star}$  in Fig. 8b. The  $R < 2.5''$  region is excluded from the fit to minimise the effects of the PSF. A thorough morphological analysis should be carried out in 2D and account for PSF smearing, as well as consider a more general Sérsic function, but the crude approach employed here suffices for our current purposes.

The bulge effective radii obtained from the fits are  $R_e = 0.26\text{ HLR}$  for the  $\mathcal{L}_{5635\text{\AA}}$  profile and  $0.24\text{ HLR}$  for  $\Sigma_{\star}$  (both of the same order of the PSF width, and so not well resolved), while the disk scales are  $h = 1.14\text{ HLR}$  for  $\mathcal{L}_{5635\text{\AA}}$  and  $1.28\text{ HLR}$  for  $\Sigma_{\star}$ . It thus seems that the structures have approximately the same sizes whether measured in light or in mass. The relative bulge-to-disk intensity scales, however, change substantially from the  $\mathcal{L}_{5635\text{\AA}}$  to the  $\Sigma_{\star}$  fits, as indeed visually evident comparing the vertical scales in Figs. 8a and b. The bulge-to-total ratios implied by the fits are  $B/T = 0.39$  in light and  $0.55$  in mass. In other words, the bulge is more relevant in mass than in light, as expected from its older stellar populations (see Fig. A1) and thus larger mass-to-light ratios.

These differences imply that this galaxy is more compact in mass than in light. A convenient and simple way of quantifying this effect is by comparing the half light and half mass radii (HLR and HMR, respectively). The HMR can be computed using  $\Sigma_{\star}$ , finding the distance where the cumulative sum of the mass reaches half of its total value. For CALIFA 0127 we obtain  $\text{HLR} = 11.4''$  and  $\text{HMR} = 8.5''$ , as indicated by the dashed vertical lines in Fig. 8. This galaxy is thus some 25% more compact in mass than in light, as indeed found for most CALIFA galaxies (González Delgado et al. 2015c).

Interestingly, Fig. 8b shows that the bulge and disk components have almost exactly the same  $\Sigma_{\star}$  at  $R = 1\text{ HMR}$ . Thus, at least for this galaxy,  $R = 1\text{ HMR} = 0.75\text{ HLR}$  is a good place to divide the galaxy into bulge and disk-dominated regions. Previous work by our group complies with this recipe, treating regions within  $0.5\text{ HLR}$  as bulge-dominated and those at  $R > 1\text{ HLR}$  as disk-dominated (González Delgado et al. 2014b).

## 5.2 Examples of usage for many galaxies

While there is much to be learned examining a single galaxy from the sample, the true power of the catalogue becomes evident when we combine large chunks of it. To illustrate this, we begin by investigating half mass and half light radii for all galaxies in the sample. Then we move to a little processing, combining radial profiles of all galaxies and deriving a mass–metallicity relation. We finish this section obtaining a Schmidt–Kennicutt-like relation for a subsample of spiral galaxies.

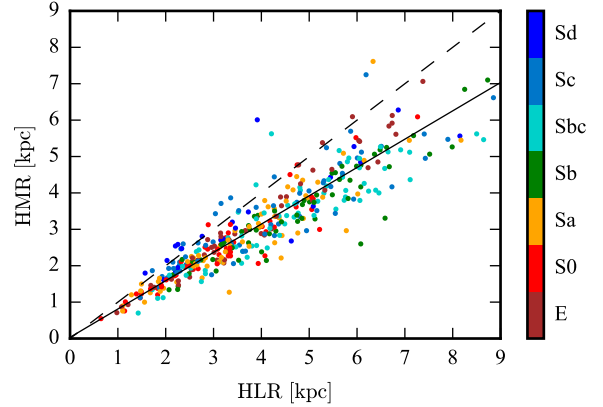


**Figure 9.** Half Mass Radius (HMR) versus Half Light Radius (HLR) for all galaxies in the sample. The  $y = x$  line is shown as a black dashed line, while the best linear fit is shown as a continuous black line. The color of the points denotes the morphological type.

### 5.2.1 Half mass vs. half light radii

As discussed at the end of Section 5.1.2, stellar mass and light are not equally distributed spatially. González Delgado et al. (2015c) have previously compared the HLR and HMR radii of 312 CALIFA galaxies.

Fig. 9 updates that previous result, now for all 395 galaxies in our database, and with the slight changes in the reduction pipeline and STARLIGHT analysis described in Section 3. The plot shows HMR and HLR for each galaxy in the sample. For most galaxies,  $\text{HMR} < \text{HLR}$ . A linear fit is drawn as a black line. We find that the galaxies are on average 22% more compact in mass. The difference goes from 18% for elliptical galaxies up to 25% for Sbc galaxies, and decreasing again to 7% for Sd galaxies, in agreement with the results reported by González Delgado et al. (2015c) for a smaller sample.

### 5.2.2 Local relations: stellar mass surface density, age, and metallicity

Galaxies come in various shapes and sizes. If we wish to combine and analyse all the galaxies in the sample, we have to somehow homogenise the data. One such way is to take mean radial profiles of the maps, using the HLR as a spatial scale. We use radial bins of  $0.1\text{ HLR}$ , from 0 to  $2.5\text{ HLR}$ . As seen in Section 5.1.1, we also take the ellipticity and orientation into account.

By using the radial profiles of the maps  $\Sigma_{\star}$  and  $\langle \log Z \rangle_{\text{M}}$ , we can build a mass–metallicity relation (MZR), as seen in Fig. 10a. The color of the bins represents the mean value of  $\langle \log t \rangle_{\text{L}}$ . This plot reproduces one of the results presented by González Delgado et al. (2014b, figure 2). There we used radial profiles of 300 galaxies. Here we update that result for 395 galaxies from the main sample.

In the bottom panel we show a similar plot, using  $\Sigma_{\star}$  and  $\langle \log t \rangle_{\text{L}}$ , with colors representing the radial distance in HLR units. The white line shows the mean value of stellar metallicity (top) and age (bottom) in bins of mass surface density. The region where the MZR is steeper corresponds

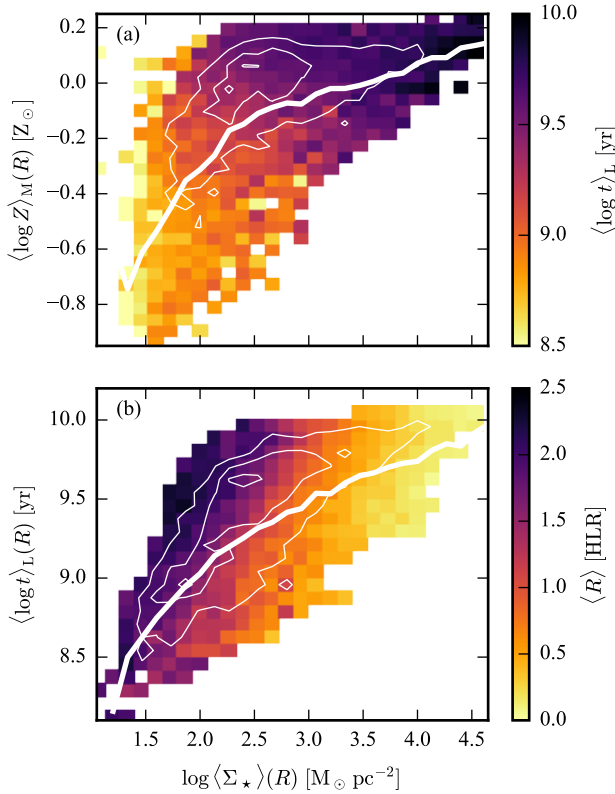


**Figure 10.** Panel (a) Mass–metallicity relation using radial profiles of  $\langle \log Z \rangle_M$  and  $\Sigma_\star$ , for all galaxies in the sample. The radial bins cover 0 to 2.5 HLR in steps of 0.1 HLR. The background tiles are the mean stellar age in 2D bins. Panel (b) The same as panel (a), but for  $\langle \log t \rangle_L$  as a function of  $\Sigma_\star$ , with colors representing the mean for the mean radial distance. The contours of the density of points is shown in thin white lines, and the mean value of stellar metallicity and age, in bins of mass surface density, is shown as a thick white line, in both panels.

to the outer parts of the galaxies, which also tend to be less dense and have younger stellar populations. The MZR becomes flatter in the inner and more dense parts, where the stellar populations are older.

### 5.2.3 The $\Sigma_{\text{SFR}}-\tau_V$ relation: A proxy for the SK law

One of the most important relations in galaxy studies is the so called Schmidt-Kennicutt (SK) law, which relates  $\Sigma_{\text{SFR}}$  to surface gas densities (Kennicutt & Evans 2012). Our STARLIGHT-based estimates of  $\Sigma_{\text{SFR}}$  differ from conventional ones, like those based on the  $\text{H}\alpha$  luminosity or the far-infrared emission, but at least we have a direct estimate of  $\Sigma_{\text{SFR}}$ . The same cannot be said about the gas surface density  $\Sigma_{\text{gas}}$ , the  $x$ -axis in the SK law, which requires measurements of the cold gaseous component in galaxies.

We do, however, have  $\tau_V$  at hand. Interpreting it as a proper dust optical depth and making some assumption about grain sizes one may derive dust column densities. Further assuming a constant dust-to-gas ratio one has that  $\tau_V \propto \Sigma_{\text{gas}}$ . These are all bold and highly questionable as-

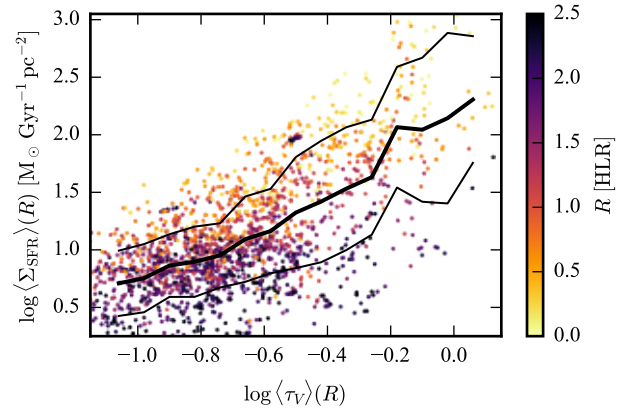


**Figure 11.** Star formation rate surface density *versus* the dust extinction (both obtained from our STARLIGHT analysis) for 98 face-on spiral galaxies, as derived from images provided in our database. The points are radial means, taken in bins of 0.1 HLR, up to 2.5 HLR. The color of the points codes for the distance of the bin to the center of the galaxy, in units of HLR. The mean value of  $\log \langle \Sigma_{\text{SFR}} \rangle$  in bins of  $\log \langle \tau_V \rangle$  is shown as a thick black line, with  $1\sigma$  range drawn as thin lines. The slope of this line,  $\sim 1.3$ , is proxy for a Schmidt-Kennicutt relation.

sumptions, of course. Nevertheless they prompt us to investigate the relation between  $\Sigma_{\text{SFR}}$  and  $\tau_V$ .

In order to do this we first select a subsample of 98 galaxies classified as spiral, non-interacting, with an ellipticity  $< 0.2$  – that is, close to being face-on. These galaxies are processed in the same way as the previous section, by calculating radial profiles of  $\Sigma_{\text{SFR}}$  and  $\tau_V$ . Fig. 11 shows the results, with the color of the points encoding the radial distance (in HLR units). The black line shows the mean value of mean star formation rate in bins of  $\tau_V$ , with a  $\pm 1\sigma$  range drawn as thin black lines. If we fit a line to the points, we obtain a slope of  $\sim 1.3$ . This is amazingly close to the slope of the SK relation (Kennicutt & Evans 2012). A preliminary version of this same relation was presented in Cid Fernandes et al. (2015, figure 3).

## 6 COMBINING DATA FROM OTHER SOURCES

The combination of our PyCASSO maps with data from other sources should be useful both as an external test on the consistency of the properties offered in our catalogue, and as a way to gain insight into physical processes within galaxies. In this section we explore both approaches. We start by comparing the stellar surface mass densities presented here with those obtained from near-IR imaging (Section 6.1). We then combine our stellar population properties with emission line data to test our SFR estimates and to exemplify how to explore the complementarity of these independent sources of information (Section 6.2). In both cases only publicly available data are used.



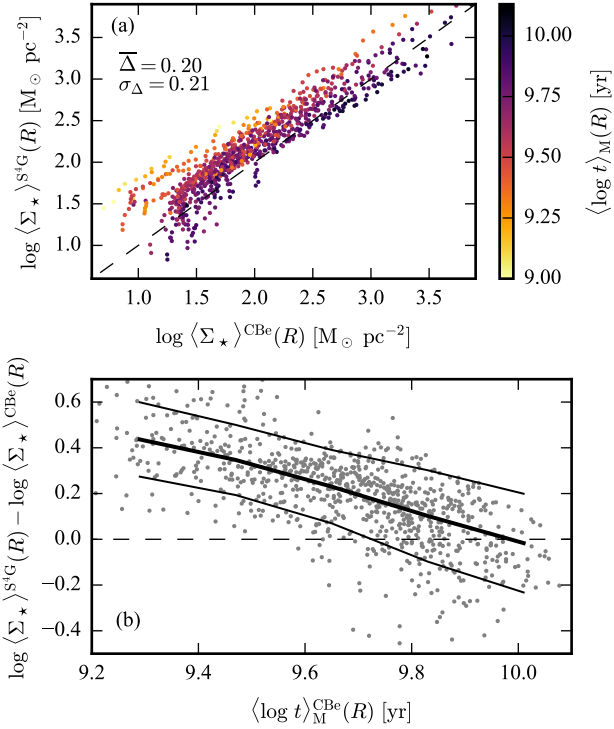


**Figure 12.** Comparison between stellar mass surface density of 35 galaxies from PyCASSO (using base *CBe*) and S<sup>4</sup>G. Each point is the average in an elliptical annulus around the centre of the galaxy. (a) S<sup>4</sup>G versus PyCASSO. The colour of the points indicates the mass-weighted mean stellar age,  $\langle \log t \rangle_{\text{M}}$ . (b) Difference between the (logarithmic) masses in both samples, as a function of mass-weighted mean stellar age. The thick black line shows the median in bins of age, and the thin lines indicate the  $\pm 1\sigma$  dispersion.

### 6.1 Mass maps from S<sup>4</sup>G

The *Spitzer* Survey of Stellar Structure in Galaxies (Sheth et al. 2010, S<sup>4</sup>G) produced, among other results, maps of the mass in old stars, through imaging in the 3.6 and 4.5  $\mu\text{m}$  bands. We found 35 galaxies present in both PyCASSO and S<sup>4</sup>G catalogues. In order to compare their  $\Sigma_{\star}$  maps to ours we first downloaded their dust-free surface brightness maps at 3.6  $\mu\text{m}$  ( $S_{3.6\mu\text{m}}$ ). As prescribed by Querejeta et al. (2015), a mass-to-light ratio  $M/L_{3.6\mu\text{m}} = 0.6 \text{M}_{\odot} L_{\odot}^{-1}$  was used to transform  $S_{3.6\mu\text{m}}$  to stellar surface mass densities. The images were then aligned to ours assuming the centroids in the infrared and optical are at the same position, and radial profiles  $\Sigma_{\star}^{\text{S}^4\text{G}}(R)$  were computed exactly as described in Section 5.1.1.

The comparison between the mass surface density from our catalogue and S<sup>4</sup>G is shown in Fig. 12. Because S<sup>4</sup>G assumes a Chabrier IMF, we use the *CBe* base maps. On average these completely independent estimates of  $\Sigma_{\star}$  differ by 0.20 dex, with an rms of 0.21 dex, compatible with the expected uncertainties of 0.08 and 0.1 dex from STARLIGHT and S<sup>4</sup>G, respectively.

There is, however, a clear trend for the difference to increase as  $\Sigma_{\star}$  decrease. The mass-weighted mean stellar age

( $\langle \log t \rangle_{\text{M}}$ ), coded by the colours in Fig. 12a, help us understand what is behind this trend. As shown in Fig. 12b, the S<sup>4</sup>G and PyCASSO masses are essentially identical as when  $\sim 10^{10}$  yr populations dominate the mass in stars. As the contribution of younger populations increases the two estimates start to diverge, reaching a difference of  $\sim 0.4$  dex in the extreme cases. The excellent agreement in  $\Sigma_{\star}$  for large values of  $\langle \log t \rangle_{\text{M}}$  is expected, as Querejeta et al. (2015) assumes the light in 3.6  $\mu\text{m}$  comes from old populations, a hypothesis which is encoded in the constant value adopted for  $M/L_{3.6\mu\text{m}}$ . The offset for younger regions is not much larger than the expected uncertainties in the  $\Sigma_{\star}$  estimates, and can be improved with a small age-dependent correction to  $M/L_{3.6\mu\text{m}}$ .

### 6.2 Emission lines from Pipe3D

Pipe3D (Sánchez et al. 2016b) is a pipeline that derives stellar and ionised gas properties from IFS. It uses FIT3D (Sánchez et al. 2016a), a spectral synthesis tool, to model the stellar continuum. The results of Pipe3D applied to 200 galaxies (V500 setup) from CALIFA DR2 (García-Benito et al. 2015) are publicly available at the CALIFA web site<sup>10</sup>. We combine the emission line results from Pipe3D to PyCASSO stellar data to explore the gas properties in relation to those of the underlying stellar populations.

When considering a combination of PyCASSO and Pipe3D data, some issues should be noted. The data reduction changed from CALIFA DR2 to DR3. The cubes are not spatially compatible. The techniques used in Pipe3D were implemented independently of this work. Also, Pipe3D used V500 cubes, while we used COMBO cubes. All these characteristics mean that, while using data from the same survey, Pipe3D and PyCASSO are datasets different enough so that a comparison between them is not trivial.

To match the cubes from both sources, we take a  $58 \times 58$  pixels slice around the reference pixel in each FITS file, taking advantage of the same pixel scale and orientation in both cases. This allows us to compare results pixel by pixel<sup>11</sup>, as well as using radial bins. We exclude galaxies that are morphologically irregular or interacting to avoid problems with the centroid in the reference pixel. The final selection contains 166 galaxies present in both samples.

#### 6.2.1 Star formation rates

As a first application, we may obtain the SFR from the maps of H $\alpha$  emission. This is a measurement of SFR using a region of spectra that is ignored by STARLIGHT, being a totally independent measurement. It is therefore instructive to compare these two estimates, following Asari et al. (2007). This is the first time this type of study is done for spatially resolved data.

The SFR is directly converted from H $\alpha$  luminosity using the standard linear relation from Kennicutt (1998), the

<sup>10</sup> CALIFA science dataproducts available at [http://www.caha.es/CALIFA/public\\_html/?q=content/science-dataproducts](http://www.caha.es/CALIFA/public_html/?q=content/science-dataproducts).

<sup>11</sup> Pipe3D used Voronoi binning in its analysis, but the actual location of the zones, as well as the dezonification scheme, is different from the ones used in PyCASSO.

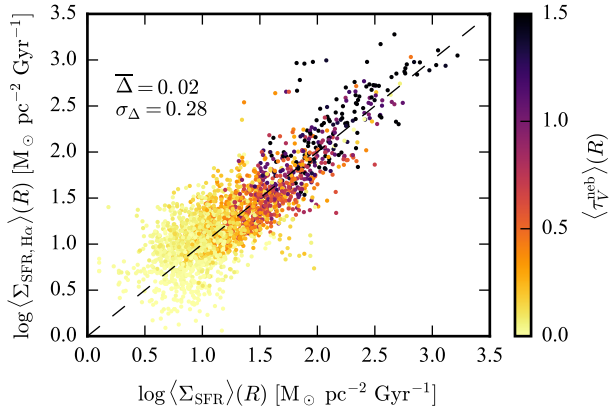


**Figure 13.** Comparison between the star formation rate surface density from 166 galaxies in PyCASSO and Pipe3D catalogues. Each point represents an elliptical annulus around the nucleus, going from 0 to 2.5 HLR in steps of 0.1 HLR. The points are coloured according to the mean nebular attenuation.

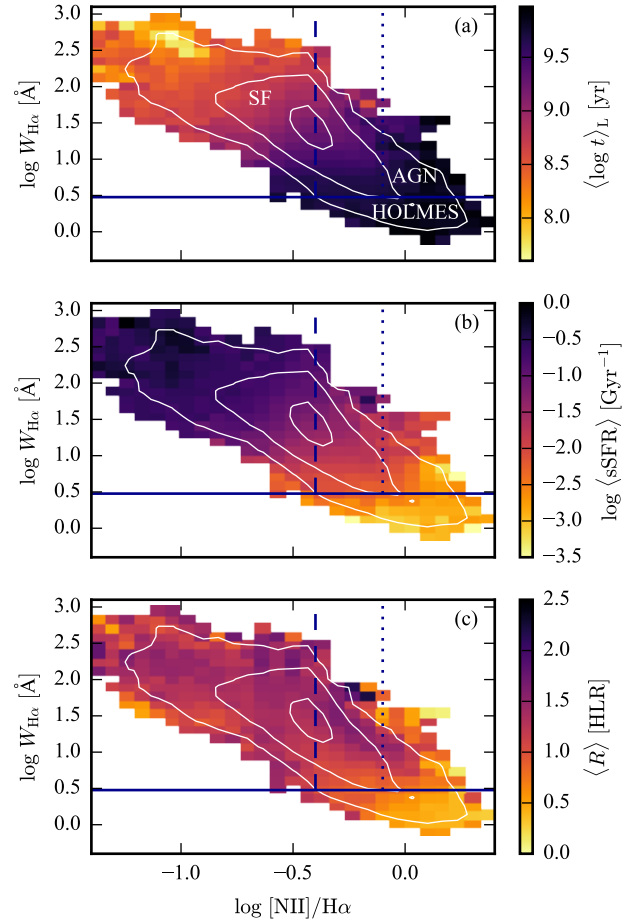
same used by [Sánchez et al. \(2016b\)](#) to compare their results to other works. The  $H\alpha$  fluxes are first corrected for dust attenuation using the [Cardelli, Clayton & Mathis \(1989\)](#) law, with  $R_V = 3.1$ . In this process, we assume an intrinsic ratio  $H\alpha/H\beta = 2.86$ . We mask pixels where  $S/N < 5$  in  $H\alpha$  or  $H\beta$ . Pixels where  $W_{H\alpha} < 14 \text{ \AA}$  are also masked, to ensure the  $H\alpha$  emission is dominated by star formation (Lacerda et al., in prep.). The dereddened  $H\alpha$  surface brightness translates straightforwardly to  $\Sigma_{SFR,H\alpha}$ , which is then averaged in radial bins of 0.1 HLR, between 0 and 2.5 HLR.

Fig. 13 compares  $\Sigma_{SFR,H\alpha}$  with our STARLIGHT-based  $\Sigma_{SFR}$ . The values from both sources agree remarkably well, with virtually no offset. The scatter in this plot, 0.28 dex, is close to the estimated uncertainty of  $\Sigma_{SFR}$  in Table 3. Points in Fig. 13 are colour-coded by  $\tau_V^{\text{neb}}$ , the optical depth derived from the observed Balmer decrement. We see that  $\tau_V^{\text{neb}}$  increases with increasing  $\Sigma_{SFR}$ , as expected from the pseudo Schmidt-Kennicutt law previously investigated in Fig. 11 in the context of stellar properties alone. This remarkable agreement gives us confidence that the SFR from the PyCASSO database can be used not only for star-forming galaxies, but for other types of galaxies where  $H\alpha$  is unrelated to star formation.

### 6.2.2 The WHAN diagram

Still using Pipe3D data, we explore the classification scheme in the WHAN diagram, which plots the equivalent width of  $H\alpha$  ( $W_{H\alpha}$ ) as a function of the ratio between the fluxes in the lines of  $[\text{N II}]\lambda 6584$  and  $H\alpha$ . This is a diagnostic diagram proposed by [Cid Fernandes et al. \(2011\)](#) to distinguish among the main ionisation sources behind galaxy spectra. Star formation (SF) and active galactic nuclei (AGN) are separated by vertical lines (constant  $[\text{N II}]/H\alpha$ ) in this diagram, while sources located below  $W_{H\alpha} = 3 \text{ \AA}$  are associated to photoionisation by hot low-mass evolved stars (HOLMES).

We extrapolate the original intent of the WHAN diagram by plotting not whole galaxies, but regions of galaxies.



**Figure 14.** Histogram of equivalent width of  $H\alpha$  versus the line ratio  $[\text{N II}]/H\alpha$ , known as WHAN diagram, using all pixels (no radial binning) from 166 galaxies matched to Pipe3D maps. The colour of the bins represent the mean value of luminosity-weighted mean stellar age (panel a), specific star formation rate (panel b) and radial distance (panel c). Each bin has at least 5 data points. White contours indicate the logarithm of the density of data points. Blue lines separate the WHAN diagram in the classes SF (star-forming), AGN and HOLMES. The horizontal continuous line shows the  $W_{H\alpha} = 3 \text{ \AA}$  limit for HOLMES. The dashed and dotted vertical lines are equivalent to the [Stasińska et al. \(2006\)](#) and [Kewley et al. \(2001\)](#) SF/AGN dividing lines, respectively.

In Fig. 14 we have 2D-histograms of all pixels of the 166 galaxies matched to Pipe3D. Bin colours in each panel represent the average luminosity-weighted stellar age ( $\langle \log t \rangle_L$ , panel a), specific star formation rate (sSFR, panel b) and distance to the nucleus in units of HLR (panel c); only bins with 5 points or more are plotted. Contours show the logarithm of the density of points. The  $W_{H\alpha} = 3 \text{ \AA}$  line separating HOLMES-ionised gas (HIG) from SF and AGN regions is indicated. Lines at  $[\text{N II}]/H\alpha = -0.4$  and  $-0.1$  separate SF from AGN regions according to the criteria of [Stasińska et al. \(2006\)](#) and [Kewley et al. \(2001\)](#), respectively, as explained in [Cid Fernandes et al. \(2010\)](#).

In Fig. 14a we can see that the HOLMES-dominated regions in the WHAN diagram is composed of old stellar populations. Those regions also have the lowest sSFR, as

seen in Fig. 14b. This might not be surprising, since  $W_{H\alpha}$  is a proxy for sSFR. This is only true, however, for systems where  $H\alpha$  is produced by H II regions. In contrast, the sSFR measured from the stellar continuum can be used to estimate star formation rates in systems where  $H\alpha$  is dominated by radiation fields other than young stars, such as AGN and HOLMES. Fig. 14c shows that the region in the WHAN diagram dubbed AGN is populated not only by the nuclear parts of galaxies, but also by off-nuclear regions. We expect those at low  $R$  to be *bona fide* AGN, while at higher  $R$  the ionisation field is most likely a mixture of H II regions and HOLMES (see Lacerda et al., in prep).

## 7 CONCLUSIONS

We have presented a value-added catalogue, publicly available at <http://pycasso.ufsc.br/>, for CALIFA galaxies analysed with the spectral synthesis code STARLIGHT and the PyCASSO pipeline. The CALIFA IFS sample is representative of galaxies in the local universe at  $0.005 < z < 0.03$ . Our catalogue is comprised of 445 galaxies from the CALIFA Data Release 3 with COMBO data. From these, 395 are taken from the mother sample, the remaining are from the extended sample.

Our public data contains maps of stellar mass surface densities, mean stellar ages and metallicities, stellar dust attenuation, star formation rates, and kinematics. We have provided a road map on how to read and interpret each physical-property image on our catalogue, and given a few examples of how to access the data in the electronic files. Since our analysis is based on spectra that have been binned with Voronoi tessellation to increase the signal-to-noise ratio, we also discuss how one may dezonify (or pixelize) the information on Voronoi zones.

We have also shown how to obtain radial profiles from our maps. Radial profiles are useful representations of two-dimensional maps, and we showcase their usefulness by separating a galaxy's bulge and disk both in its light and stellar mass profiles. This case study agrees with our previous results (González Delgado et al. 2015c) that galaxies are more compact in mass than in light.

We have used our catalogue to update and revisit a few of our former results, like the relation between half mass and half light radii, and local relations between stellar mass surface density, age, and metallicity. A few previously unexplored results were also presented, like a pseudo Schmidt–Kennicutt relation between the SFR surface density and the dust optical depth obtained using only stellar continuum information.

Finally, in order to illustrate the potential of the catalogue when used in conjunction with complementary information from other databases, we have combined it with publicly available data from the S<sup>4</sup>G and Pipe3D databases. Using emission line measurements for 166 galaxies from Pipe3D we compare the specific star formation rate from the stellar continuum to that obtained from  $H\alpha$ , finding that the two agree to within a factor of 2. We also investigate how galaxy pixels populate the WHAN diagram, which can distinguish the ionisation by SF, AGN or HOLMES in full galaxies. We show that the HOLMES/SF scenario is compatible with the stellar population ages and sSFR in the Py-

CASSO database. These example applications demonstrate the catalogue should be a useful tool to gain insight into galaxy physics.

## ACKNOWLEDGEMENTS

ALA, NVA, RCF and EADL acknowledge the support from the CAPES CsF–PVE project 88881.068116/2014-01.

CALIFA is the first legacy survey carried out at Calar Alto. The CALIFA collaboration would like to thank the IAA-CSIC and MPIA-MPG as major partners of the observatory, and CAHA itself, for the unique access to telescope time and support in manpower and infrastructures. We also thank the CAHA staff for the dedication to this project.

We thank the support from the Spanish Ministerio de Economía y Competitividad, through projects AYA2016-77846-P, AYA2014-57490-P, AYA2010-15081, and Junta de Andalucía FQ1580. We also thank the Viabilidad, Diseño, Acceso y Mejora funding program, ICTS-2009-10, for funding the data acquisition of this project. ALdA, EADL, and RCF thanks the hospitality of the IAA and the support of CNPq. RGD acknowledges the support of CNPq.

We thank the referee for comments which substantially improved this manuscript.

This research made use of Astropy, a community-developed core Python package for Astronomy (Astropy Collaboration et al. 2013).

## REFERENCES

- Abazajian K. N., et al., 2009, *ApJS*, **182**, 543  
 Alongi M., Bertelli G., Bressan A., Chiosi C., Fagotto F., Greggio L., Nasi E., 1993, *A&AS*, **97**, 851  
 Andrews B. H., Martini P., 2013, *ApJ*, **765**, 140  
 Asari N. V., Cid Fernandes R., Stasińska G., Torres-Papaqui J. P., Mateus A., Sodr e L., Schoenell W., Gomes J. M., 2007, *MNRAS*, **381**, 263  
 Astropy Collaboration et al., 2013, *A&A*, **558**, A33  
 Bian W.-H., Chen Y.-M., Gu Q.-S., Wang J.-M., 2007, *ApJ*, **668**, 721  
 Bressan A., Fagotto F., Bertelli G., Chiosi C., 1993, *A&AS*, **100**, 647  
 Bruzual G., Charlot S., 2003, *MNRAS*, **344**, 1000  
 Bundy K., et al., 2015, *ApJ*, **798**, 7  
 Cappellari M., Copin Y., 2003, *MNRAS*, **342**, 345  
 Cardelli J. A., Clayton G. C., Mathis J. S., 1989, *ApJ*, **345**, 245  
 Chabrier G., 2003, *ApJ*, **586**, L133  
 Charbonnel C., Meynet G., Maeder A., Schaller G., Schaerer D., 1993, *A&AS*, **101**, 415  
 Cid Fernandes R., Mateus A., Sodr e L., Stasińska G., Gomes J. M., 2005, *MNRAS*, **358**, 363  
 Cid Fernandes R., Asari N. V., Sodr e L., Stasińska G., Mateus A., Torres-Papaqui J. P., Schoenell W., 2007, *MNRAS*, **375**, L16  
 Cid Fernandes R., et al., 2009, in *Revista Mexicana de Astronomía y Astrofísica Conference Series*. pp 127–132  
 Cid Fernandes R., Stasińska G., Schlickmann M. S., Mateus A., Vale Asari N., Schoenell W., Sodr e L., 2010, *MNRAS*, **403**, 1036  
 Cid Fernandes R., Stasińska G., Mateus A., Vale Asari N., 2011, *MNRAS*, **413**, 1687  
 Cid Fernandes R., et al., 2013, *A&A*, **557**, A86  
 Cid Fernandes R., et al., 2014, *A&A*, **561**, A130

- Cid Fernandes R., et al., 2015, in Ziegler B. L., Combes F., Dannerbauer H., Verdugo M., eds, IAU Symposium Vol. 309, Galaxies in 3D across the Universe. pp 93–98 ([arXiv:1409.7400](https://arxiv.org/abs/1409.7400)), doi:10.1017/S1743921314009387
- Colless M., et al., 2001, *MNRAS*, 328, 1039
- Cortijo-Ferrero C., et al., 2017, *MNRAS*, 467, 3898
- Croom S. M., et al., 2012, *MNRAS*, 421, 872
- Fagotto F., Bressan A., Bertelli G., Chiosi C., 1994a, *A&AS*, 104
- Fagotto F., Bressan A., Bertelli G., Chiosi C., 1994b, *A&AS*, 105
- Fagotto F., Bressan A., Bertelli G., Chiosi C., 1994c, *A&AS*, 105
- Falcón-Barroso J., et al., 2017, *A&A*, 597, A48
- Galbany L., et al., 2014, *A&A*, 572, A38
- García-Benito R., et al., 2015, *A&A*, 576, A135
- Girardi L., Bressan A., Chiosi C., Bertelli G., Nasi E., 1996, *A&AS*, 117, 113
- Girardi L., Bressan A., Bertelli G., Chiosi C., 2000, *A&AS*, 141, 371
- González Delgado R. M., Cerviño M., Martins L. P., Leitherer C., Hauschildt P. H., 2005, *MNRAS*, 357, 945
- González Delgado R. M., et al., 2014a, *A&A*, 562, A47
- González Delgado R. M., et al., 2014b, *ApJ*, 791, L16
- González Delgado R. M., et al., 2015a, in Cenarro A. J., Figueras F., Hernández-Monteagudo C., Trujillo Bueno J., Valdivielso L., eds, Highlights of Spanish Astrophysics VIII. pp 220–227
- González Delgado R. M., et al., 2015b, in Ziegler B. L., Combes F., Dannerbauer H., Verdugo M., eds, IAU Symposium Vol. 309, IAU Symposium. pp 99–104
- González Delgado R. M., et al., 2015c, *A&A*, 581, A103
- González Delgado R. M., et al., 2016, *A&A*, 590, A44
- Kelz A., et al., 2006, *PASP*, 118, 129
- Kennicutt Jr. R. C., 1998, *ARA&A*, 36, 189
- Kennicutt R. C., Evans N. J., 2012, *ARA&A*, 50, 531
- Kent S. M., 1985, *ApJS*, 59, 115
- Kewley L. J., Dopita M. A., Sutherland R. S., Heisler C. A., Trevena J., 2001, *ApJ*, 556, 121
- Koleva M., Prugniel P., Ocvirk P., Le Borgne D., Soubiran C., 2008, *MNRAS*, 385, 1998
- Kormendy J., 1977, *ApJ*, 217, 406
- Lara-López M. A., Cepa J., Bongiovanni A., Castañeda H., Pérez García A. M., Fernández Lorenzo M., Póvic M., Sánchez-Portal M., 2009a, *A&A*, 493, L5
- Lara-López M. A., Cepa J., Bongiovanni A., Pérez García A. M., Castañeda H., Fernández Lorenzo M., Póvic M., Sánchez-Portal M., 2009b, *A&A*, 505, 529
- Lara-López M. A., Bongiovanni A., Cepa J., Pérez García A. M., Sánchez-Portal M., Castañeda H. O., Fernández Lorenzo M., Póvic M., 2010, *A&A*, 519, A31
- Le Borgne J.-F., et al., 2003, *A&A*, 402, 433
- Liang Y. C., Hammer F., Yin S. Y., Flores H., Rodrigues M., Yang Y. B., 2007, *A&A*, 473, 411
- López Fernández R., et al., 2016, *MNRAS*, 458, 184
- Martin D. C., et al., 2005, *ApJ*, 619, L1
- Martins L. P., González Delgado R. M., Leitherer C., Cerviño M., Hauschildt P., 2005, *MNRAS*, 358, 49
- Mateus A., Sodr e L., Cid Fernandes R., Stasińska G., Schoenell W., Gomes J. M., 2006, *MNRAS*, 370, 721
- Mateus A., Sodr e L., Cid Fernandes R., Stasińska G., 2007, *MNRAS*, 374, 1457
- Méndez-Abreu J., et al., 2017, *A&A*, 598, A32
- Ocvirk P., Pichon C., Lançon A., Thiébaud E., 2006a, *MNRAS*, 365, 46
- Ocvirk P., Pichon C., Lançon A., Thiébaud E., 2006b, *MNRAS*, 365, 74
- Panther B., Heavens A. F., Jimenez R., 2003, *MNRAS*, 343, 1145
- Panther B., Jimenez R., Heavens A. F., Charlot S., 2007, *MNRAS*, 378, 1550
- Peebles M. S., Pogge R. W., Stanek K. Z., 2009, *ApJ*, 695, 259
- Pérez E., et al., 2013, *ApJ*, 764, L1
- Querejeta M., et al., 2015, *ApJS*, 219, 5
- Riffel R., Pastoriza M. G., Rodríguez-Ardila A., Bonatto C., 2009, *MNRAS*, 400, 273
- Roth M. M., et al., 2005, *PASP*, 117, 620
- Sánchez-Blázquez P., et al., 2006, *MNRAS*, 371, 703
- Sánchez S. F., et al., 2012, *A&A*, 538, A8
- Sánchez S. F., et al., 2016a, *Rev. Mex. Astron. Astrofis.*, 52, 21
- Sánchez S. F., et al., 2016b, *Rev. Mex. Astron. Astrofis.*, 52, 171
- Sánchez S. F., et al., 2016c, *A&A*, 594, A36
- Schaerer D., Meynet G., Maeder A., Schaller G., 1993a, *A&AS*, 98, 523
- Schaerer D., Charbonnel C., Meynet G., Maeder A., Schaller G., 1993b, *A&AS*, 102, 339
- Schaller G., Schaerer D., Meynet G., Maeder A., 1992, *A&AS*, 96, 269
- Sheth K., et al., 2010, *PASP*, 122, 1397
- Stanishev V., Rodrigues M., Mourão A., Flores H., 2012, *A&A*, 545, A58
- Stasińska G., Cid Fernandes R., Mateus A., Sodr e L., Asari N. V., 2006, *MNRAS*, 371, 972
- Stasińska G., Vale Asari N., Cid Fernandes R., Gomes J. M., Schlickmann M., Mateus A., Schoenell W., Sodr e Jr. Seagal Collaboration L., 2008, *MNRAS*, 391, L29
- Stasińska G., Costa-Duarte M. V., Vale Asari N., Cid Fernandes R., Sodr e L., 2015, *MNRAS*, 449, 559
- Stoughton C., et al., 2002, *AJ*, 123, 485
- Tojeiro R., Heavens A. F., Jimenez R., Panther B., 2007, *MNRAS*, 381, 1252
- Vale Asari N., Stasińska G., Cid Fernandes R., Gomes J. M., Schlickmann M., Mateus A., Schoenell W., 2009, *MNRAS*, 396, L71
- Vazdekis A., Sánchez-Blázquez P., Falcón-Barroso J., Cenarro A. J., Beasley M. A., Cardiel N., Gorgas J., Peletier R. F., 2010, *MNRAS*, 404, 1639
- Walcher C. J., et al., 2014, *A&A*, 569, A1
- York D. G., et al., 2000, *AJ*, 120, 1579

## APPENDIX A: OTHER GALAXIES

This appendix shows a few more examples of maps available in the PyCASSO database (<http://pycasso.ufsc.br/>) presented in this paper. Figs. A1 to A8 are sorted according to morphological type, from an elliptical galaxy to a merger.

This paper has been typeset from a  $\text{\TeX}/\text{\LaTeX}$  file prepared by the author.

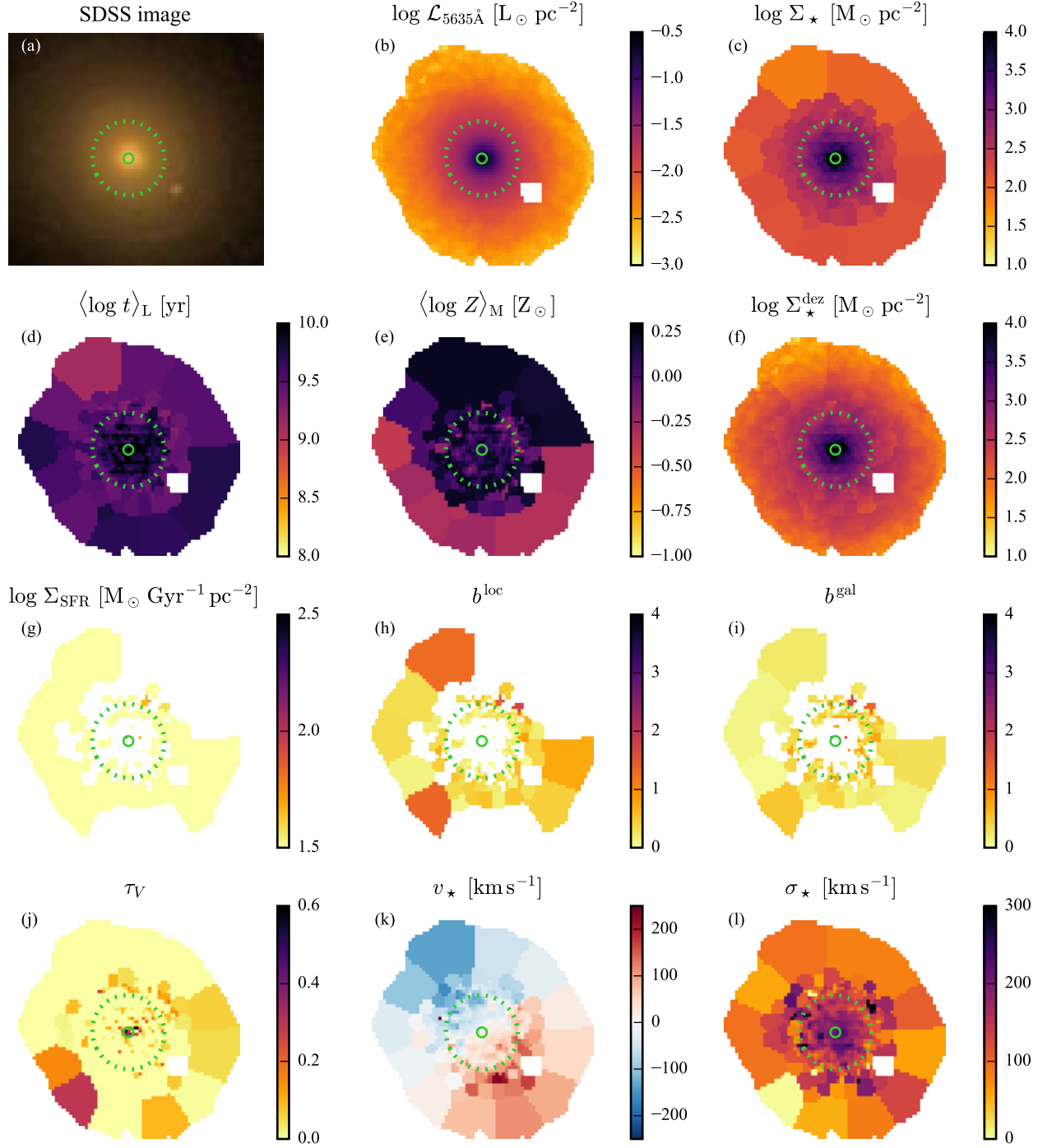


**Figure A1.** Maps of selected physical properties for the elliptical galaxy NGC 1349 (CALIFA 0127). A dotted ellipse marks the 1 HLR area.

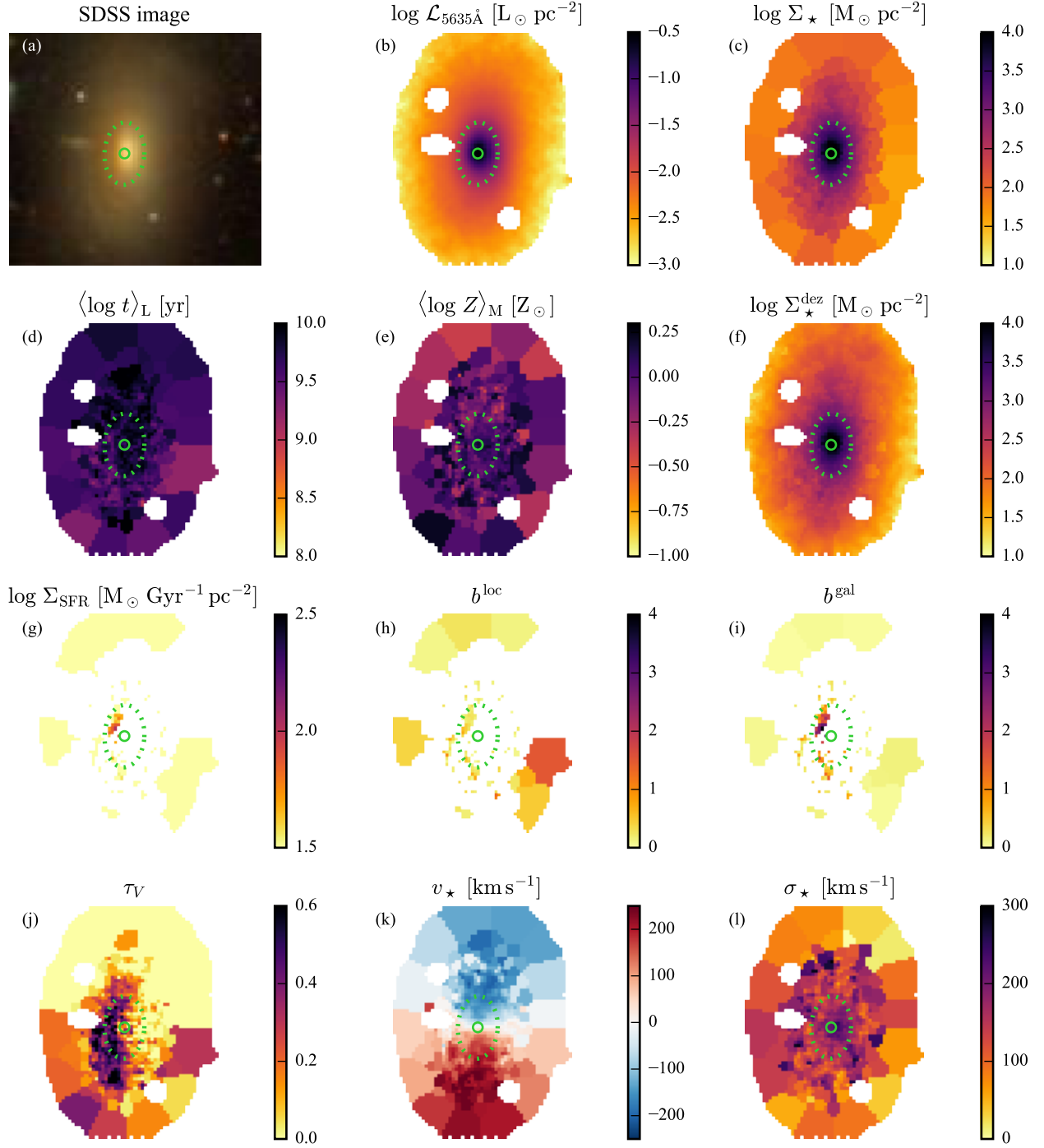


**Figure A2.** As Fig. A1, but for the S0 galaxy UGC 10905 (CALIFA 0858).

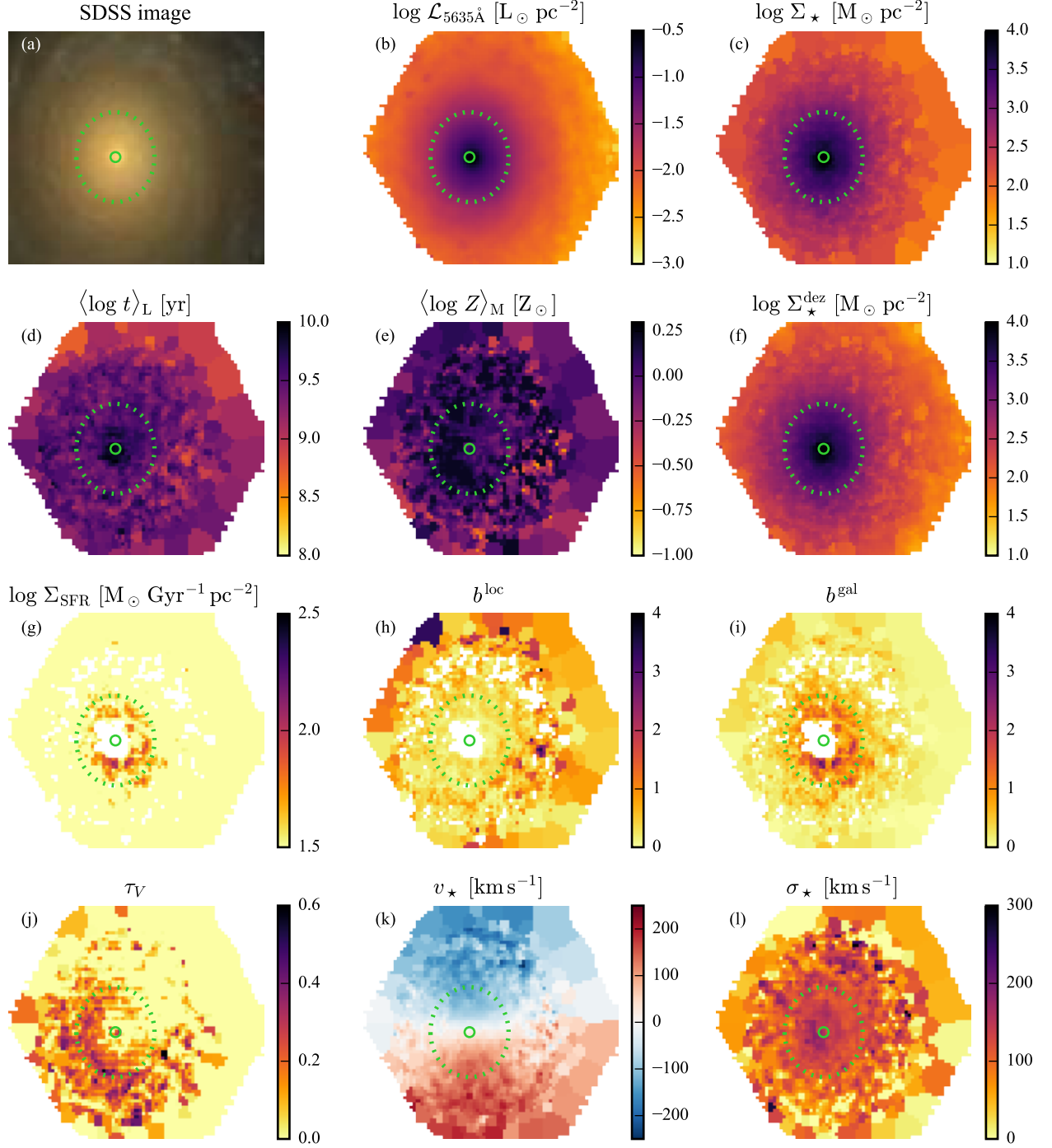


Figure A3. As Fig. A1, but for the Sa galaxy NGC 1070 (CALIFA 0102).

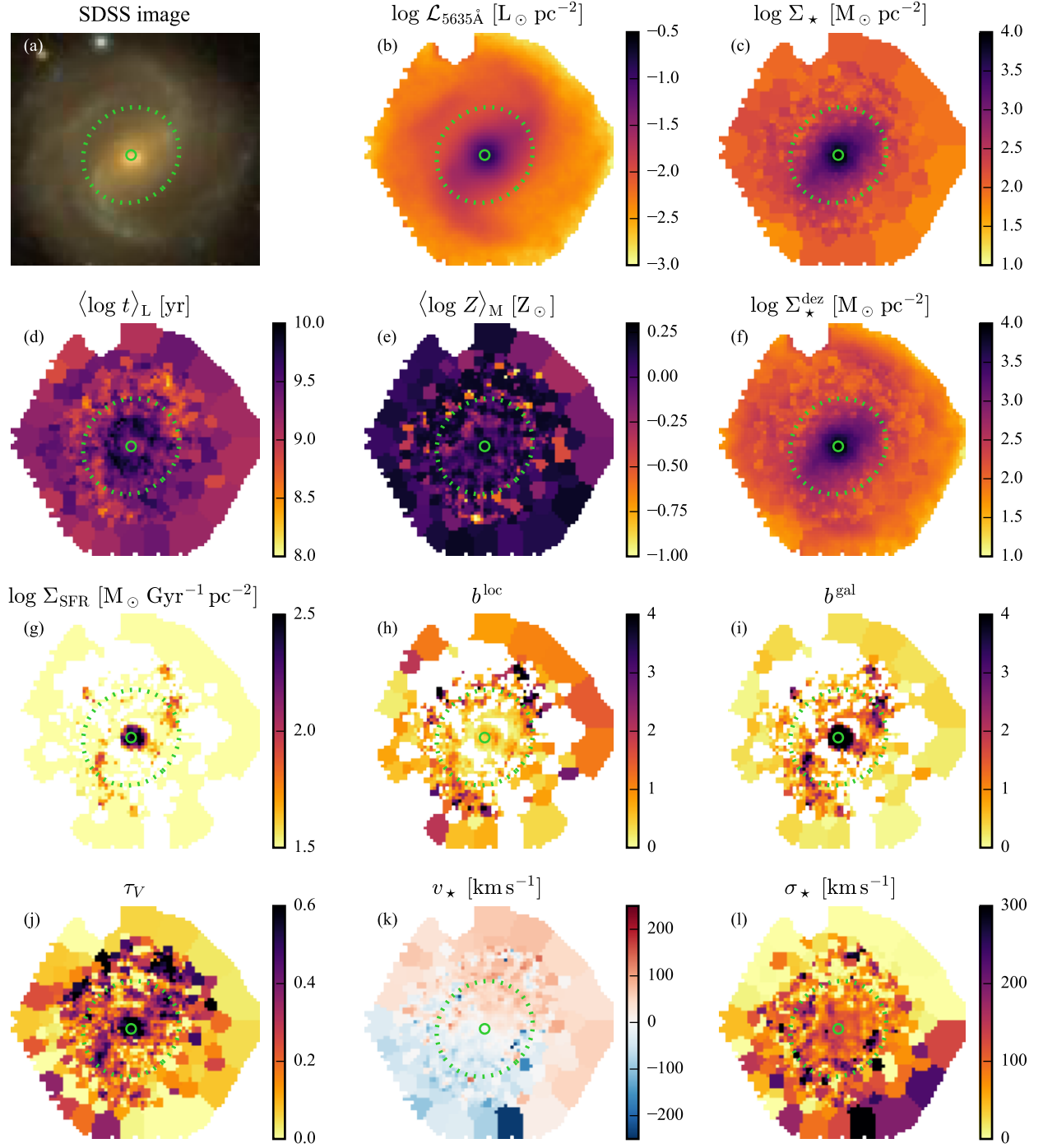


Figure A4. As Fig. A1, but for the Sb galaxy NGC 0776 (CALIFA 0073).



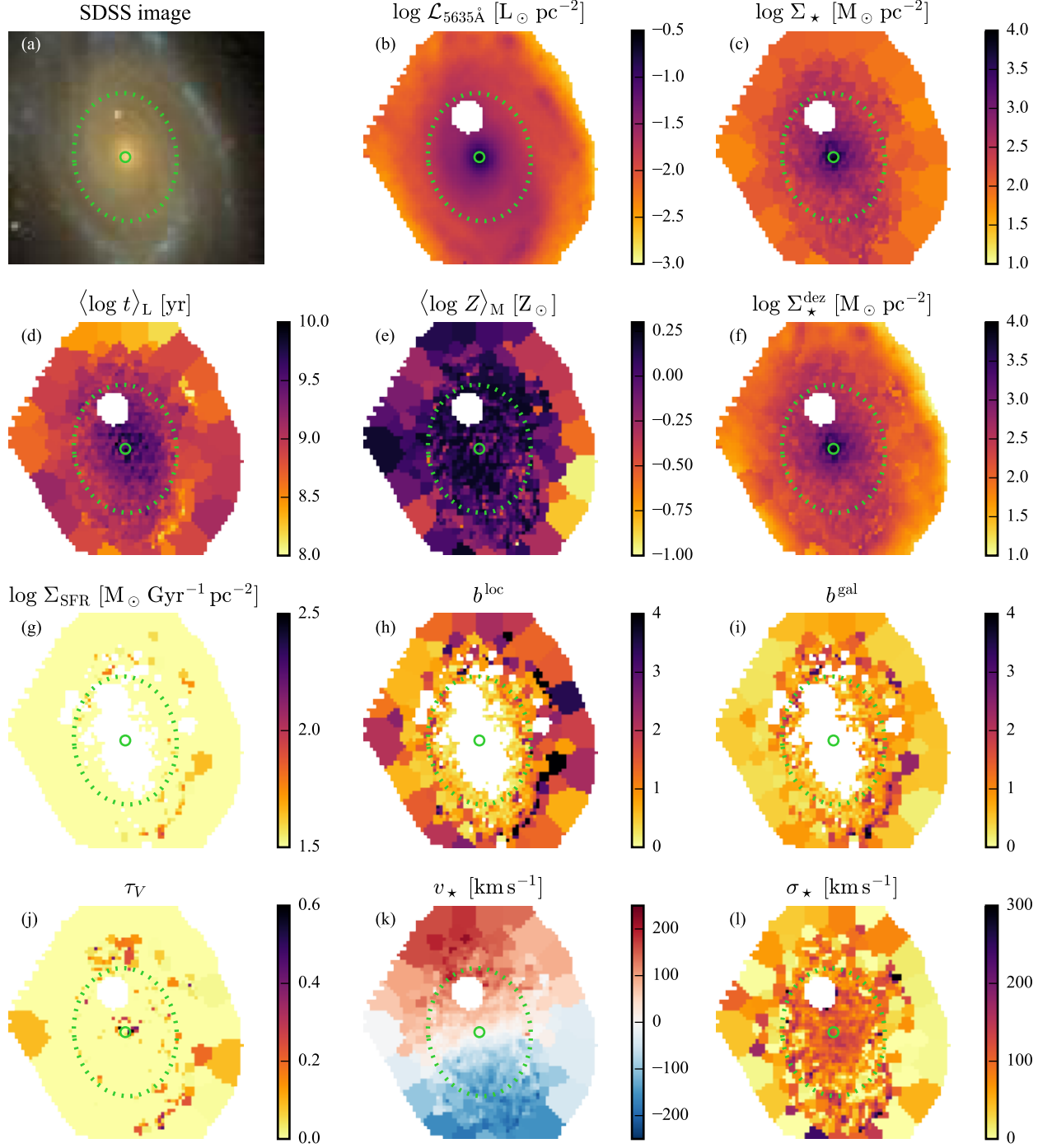
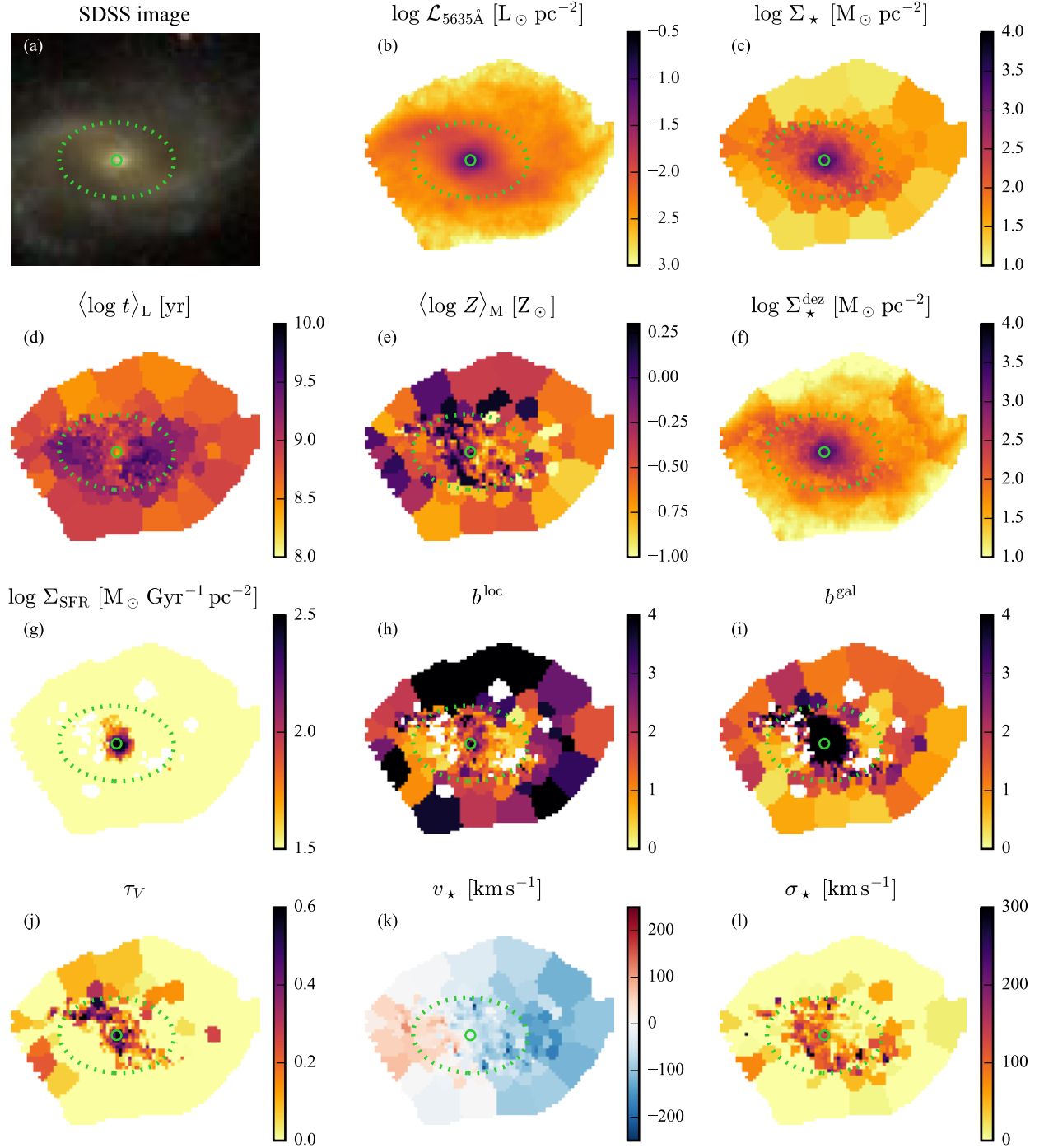


Figure A5. As Fig. A5, but for the Sbc galaxy NGC 2916 (CALIFA 0277).



**Figure A6.** As Fig. A1, but for the Sc galaxy NGC 7819 (CALIFA 0003).

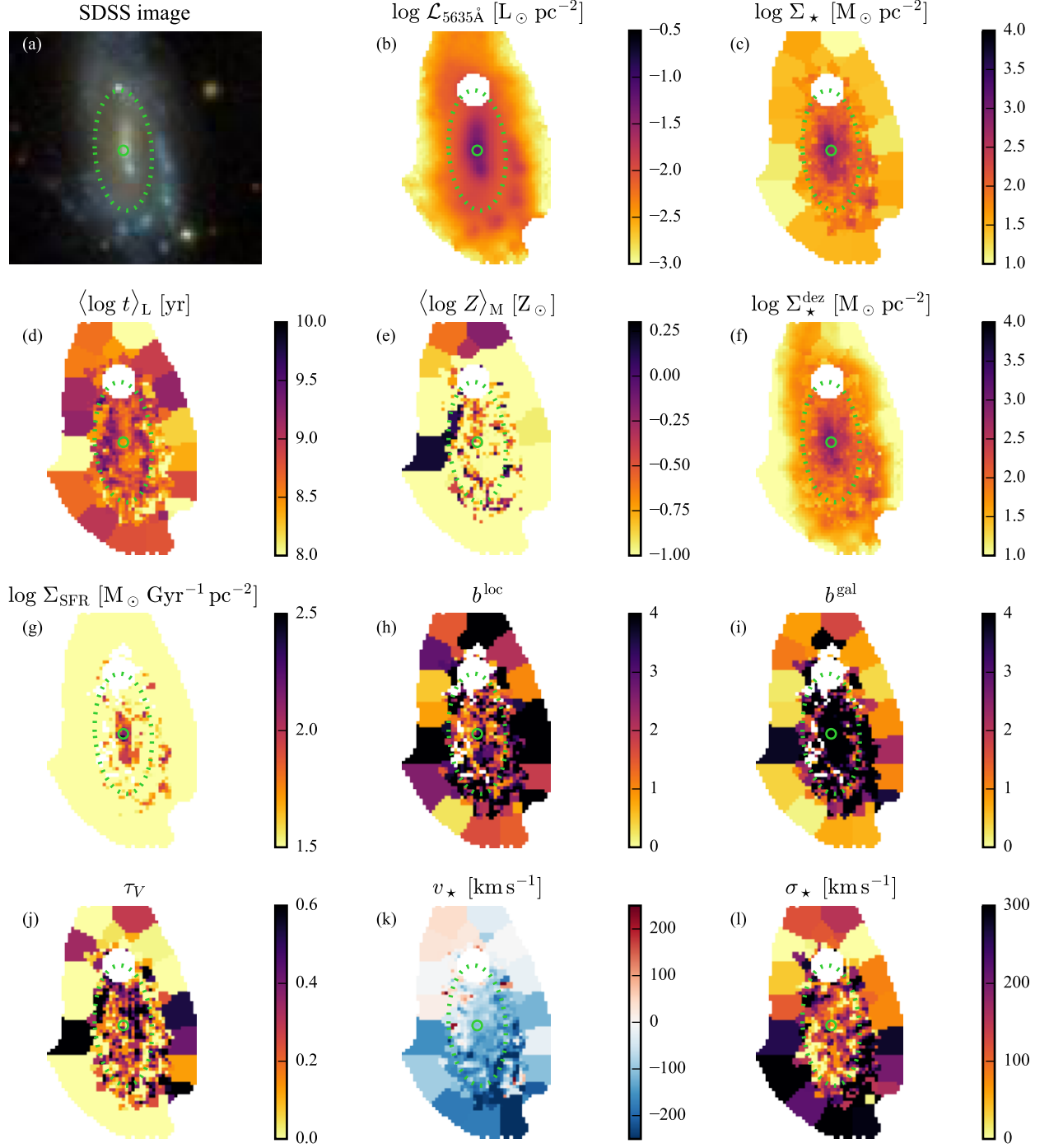
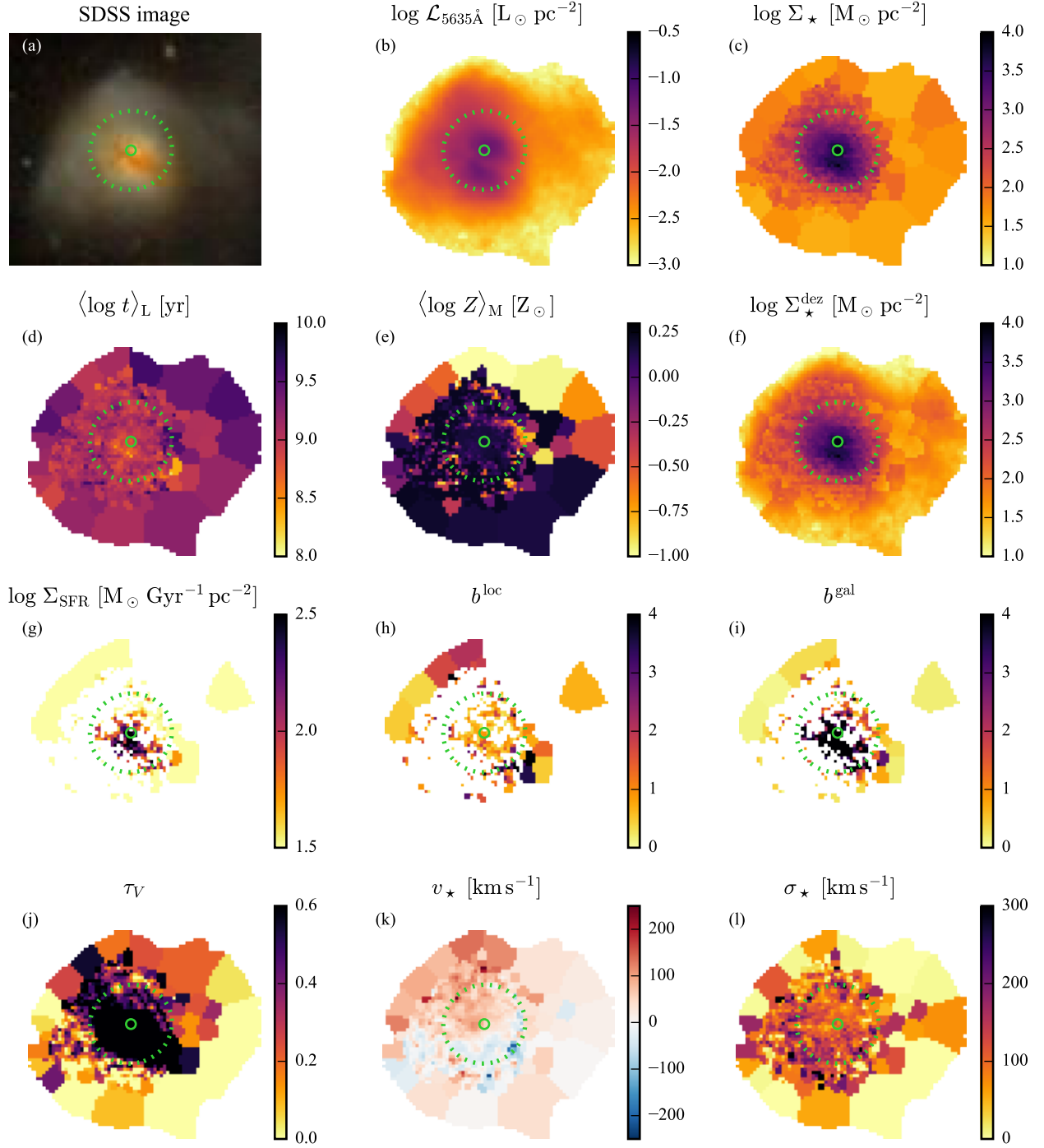


Figure A7. As Fig. A1, but for the Sd galaxy UGC 00312 (CALIFA 0014).



**Figure A8.** As Fig. A1, but for the merger system Arp 220 (CALIFA 802).